

# **InsulPatch: A Slim, Powerless Microfluidic Patch-Pump for Insulin Delivery**

Shuyu Zhang

Thesis submitted to the faculty of the Virginia Polytechnic Institute and State University in partial fulfillment of the requirements for the degree of

Master of Science

In

Biomedical Engineering

Anne E. Staples, Chair

Rafael V. Davalos

John J. Socha

Andre A. Muelenaer

May 5, 2022

Blacksburg, Virginia

Keywords: Microfluidic device, soft lithography, replica molding, 3D printing, microneedle array, drug delivery, insulin, diabetes

Copyright © 2022 by Shuyu Zhang

# **InsulPatch: A Slim, Powerless Microfluidic Patch-Pump for Insulin Delivery**

Shuyu Zhang

## **Abstract**

The InsulPatch is a novel integrated patch-pump device used to deliver drugs, especially macromolecular drugs that are difficult to deliver through an oral pathway and that require transdermal delivery. The patch-pump is a promising replacement for conventional syringes and battery-powered pumps because it is slim, powerless, painless, and relatively inexpensive. The majority of this thesis focuses on the fabrication and testing of microfluidic devices for the delivery of insulin, which is a model drug that is widely used and needs to be delivered transdermally.

In this thesis, we demonstrate the fabrication of the patch-pump, which includes an insect-mimetic microfluidic pump fabricated using photolithography and replica molding, and a microneedle array fabricated using 3D printing. The microfluidic pump is used to drive the fluid flow powered by pressurized air or the user's pulse, and the microneedle array is used to inject the fluid through the skin painlessly. Using pressurized air-driven flow testing, we have tested the flow rate across microfluidic pumps of various flow channel widths over a range of physiologically relevant actuation frequencies and pressures. We have found that for the specific channel design we have been using, the flow rate generally positively correlates with the actuation pressure. For devices with wider flow channels, the flow rate generally negatively correlates with the actuation frequency, whereas the flow rate increases and then decreases with increasing actuation frequency for devices with narrower flow channels. This property of these devices is beneficial in insulin delivery because the demand for insulin is generally reduced in vigorous exercise (with elevated heart rate/actuation frequency) and increased in hypertension patients (with elevated blood/actuation pressure).

A major future direction of the study is to test a wide range of device designs in a sample of human subjects by attaching the device onto the wrist and measuring the pulse-driven flow across the device. We can further change the channel design parameters of the device so that it will be ideal for insulin delivery. Using the *ex vivo* flow testing and human subject data, we can further tailor the device design to specific patients using a genetic algorithm-guided optimization based on the heart rate and blood pressure of the patient and the desired flow rate. We will also perform computational modeling using COMSOL Multiphysics to predict the flow across devices of different designs as well as to understand the physics behind the pulse-driven flow. Finally, a 3D-printed insulin reservoir will be incorporated into our patch-pump system for the storage of U-500 insulin.

# **InsulPatch: A Slim, Powerless Microfluidic Patch-Pump for Insulin Delivery**

Shuyu Zhang

## **General Audience Abstract**

The InsulPatch is a slim, powerless device (“patch-pump”) that can be used to deliver drugs through the skin, especially designed for drugs that are difficult to deliver orally. The patch technology is a promising replacement for conventional injection using syringes and bulky battery-powered pumps. At this stage, the primary drug that our device aims to deliver is insulin, which generally needs to be delivered through the skin.

In this thesis, we demonstrate how our patch-pump is made and how its performance is tested. The patch-pump has two parts: the microfluidic pump and the microneedle array. The microfluidic pump is fabricated using a technique called photolithography, in which a photosensitive polymer is selectively cured by UV light, and replica molding, in which the precursor of another polymer is poured on a mold and cured. The microneedle array is made using 3D printing and designed in such a way so that it can be readily connected to the microfluidic pump. The microfluidic pump is used to drive the fluid flow powered by the user’s pulse, and the microneedle array is used to inject the fluid through the skin painlessly. Through testing the flow across the microfluidic pump prototypes using pressurized air, we characterized the correlation between the flow rate of fluid across the device and parameters including the actuation pressure and frequency of the pressurized air as well as the width of the flow channel.

Future directions of the study include testing the devices in human subjects to characterize pulse-driven flow across the devices, computational modeling of the devices, and further changes of the device design to optimize the performance of the device. We will also optimize the device design computationally to tailor the device design to specific diabetic patients. Finally, we will incorporate a 3D-printed insulin reservoir into our system for the storage of insulin solution.

## Acknowledgements

A special thank you goes to my amazing advisor, Dr. Anne Staples. Without the help, encouragement, and guidance from Dr. Staples, I would not have been able to come this far in research. She has always been very caring, involved, and supportive in my project and my academic life—thank you, Dr. Staples.

Thanks to Dr. Rafael Davalos for laying a solid foundation of microchannel design and microfluidic fabrication, as well as being willing to serve on my committee.

Thanks to Dr. Jake Socha for providing the lab space and laying foundations of insect-inspired microfluidics, as well as being willing to serve on my committee. I would also like to thank Dr. Krishnashis Chatterjee, Ms. Afreen Khoja, and Ms. Demi Poulos for the preceding work in this project.

Thanks to Dr. Andre Muelenaer for being willing to serve on my committee.

Thanks to my amazing senior design team and undergraduate research assistants, Ms. Jenna Sims, Ms. Isabelle Mehochko, Mr. Tyler Kwak, Mr. Ryan Zolovick, Ms. Brea Shaeffer, Ms. Julia Frederick, Ms. Aleksandra Grodski, and Ms. Julia Wakefield for helping me on the experimental side of the project.

Thanks to experts in soft lithography, Dr. Sebastian Cargou, Ms. Josie Duncan, and Mr. Edward “Jake” Jacobs, for giving me a tremendous amount of help in device fabrication.

Finally, thanks to everyone who has played a supportive role in my project.

# Contents

Abstract	ii
General Audience Abstract	iii
Acknowledgements	iv
List of Figures	viii
List of Tables	x
1 Introduction	1
2 Materials and Methods	4
2.1 Fabrication of Microfluidic Pump	4
2.1.1 Master mold fabrication	4
2.1.2 PDMS device fabrication	4
2.1.3 Alternative device fabrication	5
2.2 Fabrication of Microneedle Arrays	5
2.3 Penetration Testing of Microneedle Arrays	6
2.4 <i>Ex Vivo</i> Flow Testing of Microfluidic Devices	7
2.4.1 Flow testing procedure	7
2.4.2 Data analysis	9
2.4.3 Flow testing experiments	9
2.4.3.1 Preliminary testing of multiple devices at three physiologically relevant actuation pressures and frequencies	9
2.4.3.2 Generation of a flow rate profile of model device across a range of physiologically relevant actuation frequencies and pressures	9
2.4.3.3 Investigation of the effect of additional components on flow rate and hydraulic resistance	10
2.4.3.4 Detailed testing of more devices and characterization of flow rate as a function of multiple variables	10
2.5 Assembly of Components into a Wearable Patch-Pump	10

2.6 Statistical Analysis	10
3 Results	12
3.1 Fabrication of Patch-Pump	12
3.1.1 Master mold fabrication	12
3.1.2 Microfluidic device fabrication	13
3.1.3 Microneedle array fabrication	14
3.2 Penetration Testing of Microneedle Arrays	18
3.3 <i>Ex Vivo</i> Flow Testing of Microfluidic Devices	20
3.3.1 Crude characterization of flow rate across microfluidic pumps at three actuation frequencies and pressures	20
3.3.2 Flow rate profile of a narrow-flow-channel model device across a spectrum with respect to actuation pressure and frequency	21
3.3.3 Flow rate profile of a narrow-flow-channel model device with additional components added	22
3.3.4 Flow rate profile of devices with various flow channel widths across physiologically relevant actuation frequency and pressure spectra	24
3.4 Assembly of an Integrated Patch-Pump Prototype	32
4 Discussion	33
4.1 Fabrication of Microfluidic Devices and Microneedle Arrays	33
4.2 Penetration testing of microneedle arrays and comparison of microneedle array prototypes	34
4.3 Flow testing across microfluidic devices	35
4.4 Limitations of Study	38
4.4.1 Fabrication of master molds and microfluidic devices	38
4.4.2 Fabrication and penetration testing of microneedle arrays	38
4.4.3 Flow testing	40
5 Conclusions and Future Directions	42
5.1 Conclusions	42
5.2 Future Directions	42

5.2.1 Further flow characterization of three-layer devices with compressed air and two-layer devices with human subjects	42
5.2.2 Optimization of device design with a genetic algorithm-guided approach	43
5.2.2.1 Genetic algorithm script	44
5.2.2.2 Model script	44
5.2.2.3 Main function	44
5.2.3 Development of a three-dimensional computational model of the device using COMSOL Multiphysics	46
5.2.4 Design and incorporation of a 3D-printed insulin reservoir	46
Bibliography	48

## List of Figures

Figure 1.1 Insect respiratory system and insect-mimetic microfluidic devices	2
Figure 2.1 Microneedle Array Penetration Testing Apparatus	7
Figure 2.2 The flow testing apparatus with pressurized air	8
Figure 3.1 Master molds fabricated using photolithography	13
Figure 3.2 Microfluidic pump design and operation	14
Figure 3.3 3D printed microneedle arrays	15
Figure 3.4 CAD prototypes of six microfluidic designs adapted for transdermal insulin delivery developed using COMSOL Multiphysics	16
Figure 3.5 Microneedle array prototypes involved in the porcine skin penetration testing	18
Figure 3.6 Penetration testing data of nine microneedle arrays	20
Figure 3.7 Characterization of flow rate across a series of microfluidic devices against actuation pressure and frequency	21
Figure 3.8 Detailed characterization of flow rate across the model device (device #2, flow channel width 2300 $\mu\text{m}$ , flow channel depth 80 $\mu\text{m}$ )	22
Figure 3.9 Detailed characterization of (a) flow rate and (b) hydraulic resistance against actuation frequency with a microneedle array and a piece of porcine skin involved	23
Figure 3.10 Detailed characterization of flow rate against actuation frequency for devices at five flow channel widths	25
Figure 3.11 Detailed characterization of flow rate against actuation pressure for devices at five flow channel widths	27
Figure 3.12 Detailed characterization of flow rate against flow channel width at five different actuation frequencies	29
Figure 3.13 Detailed characterization of flow rate against flow channel width at five different actuation pressures	31
Figure 3.14 Current Integrated Patch-Pump Prototypes	32
Figure 4.1 Limitation in current microfluidic device fabrication methods and alternative solution	34
Figure 4.2 Collapse and re-expansion of flow channel at 30 and 180 bpm	36
Figure 4.3 Delivery of red-dyed water to porcine skin through a microneedle array	39
Figure 4.4 Schematic of human subject testing and comparison of flow rates across devices at different flow channel widths actuated by compressed air and by radial arterial pulse on the human subject	41

Figure 5.1 Eleven insect-mimetic microfluidic channel designs by Chatterjee et al. (2021) and their performances at different actuation frequencies from 0 to 45 Hz	43
Figure 5.2 A genetic algorithm-guided approach to optimize the channel design	45
Figure 5.3 Finite element model of microneedle array	46
Figure 5.4 First prototype of cubic insulin reservoir design using COMSOL Multiphysics	47

## List of Tables

Table 3.1 Flow channel widths of devices produced by the current photomask/master mold system	12
Table 3.2 Shapes and dimensions of the six microneedle array prototypes	17
Table 3.3 Penetration testing data of microneedle array prototypes against porcine skin	19
Table 4.1 Estimated maximum membrane deflection for the five device designs we have used	37

# Chapter 1

## Introduction

Diabetes mellitus, or simply diabetes, is a very common disease worldwide. As of 2019, almost 500 million people worldwide were estimated to suffer from diabetes.<sup>1</sup> In the US alone, a 2019 estimate suggested that at least 37.3 million American adults had diabetes, which was more than a tenth of the population.<sup>2</sup> If we add the of diabetic and prediabetic populations in the US together, that would be over one third of the American population.<sup>2</sup> The annual budget spent on diabetes in the US was estimated at \$327 billion.<sup>3</sup>

Diabetes can be categorized as one of two types: Type 1, which is marked by targeting of auto-antibodies against insulin, and Type 2, which is marked by the impaired ability to respond to insulin secretion.<sup>4-8</sup> Recent estimates suggest that approximately 90% of diabetic patients worldwide and in the US suffer from Type 2 diabetes, while the rest suffer from Type 1.<sup>9,10</sup> For both types of diabetes, treatments are centered on delivery of exogenous insulin.<sup>11</sup> Common methods for insulin delivery include injections using a syringe that contains a macrobore cannula or continuous delivery with a powered pump.<sup>11,12</sup> Main limitations of syringe injection include injection site reactions, or pain, and the inability to achieve continuous insulin delivery, which may cause hypoglycemic crises.<sup>13-17</sup> For the powered pump, main limitations include bulkiness due to the battery in the pump and interference with physical activity (and these pumps are usually also cannula-based).<sup>11,18,19</sup> In addition, cost and embarrassment are associated with both forms of treatment. These limitations, along with the cost associated with current insulin delivery methods, lead to a devastating problem of non-adherence to treatments in diabetic patients, which can result in increases in mortality and hospitalization rates.<sup>20-25</sup> Therefore, there is a critical need to develop novel therapies that can reduce these limitations for diabetic patients.

Some alternative treatments also have been developed, yet they are still not as promising as one can expect. Oral treatments are very difficult for insulin due to the first-pass effect of the hepatic and gut wall.<sup>26,27</sup> Inhaled insulin is another potential alternative, yet it has a series of limitations—it is more expensive than injected insulin, and inhaled insulin products including Exubera and Afrezza are positively correlated with hypoglycemia, lung cancer, as well as other respiratory conditions.<sup>28-30</sup> Insulin patches have a promising potential due to their slim nature and the low amount of pain involved, but current insulin patches typically involve smart technologies or sophisticated components and therefore typically tend to be expensive.<sup>17,31,32</sup> The other limitation is that currently available patches deliver insulin in discrete boluses rather than in an automated, continuous manner.<sup>32</sup>

Our laboratory has adequate expertise in fabricating insect-mimetic microfluidic devices. Insect respiration relies on the periodic contractions of the abdomen, which rhythmically collapse and expand different parts of the tracheal tubes and therefore drive a net flow of air.<sup>33-35</sup> Chatterjee et al. (2021) from our research group harnessed this mechanism and designed three-layer single-

channel and multi-channel microfluidic devices as shown in Figure 1.1b-d.<sup>33</sup> As shown in Figure 1.1d, a pressurized air source in the form of a square wave is generated and flows into the actuation (red) channel of the top layer, and this can cause the elastomeric membrane (gray) to collapse against the flow channel (green). Due to the asymmetry of the channel design, the rhythmic contraction and re-expansion process can generate a net fluid flow. In the study described in this thesis, we aimed to apply single-channel, 3-layer microfluidic devices to the delivery of insulin by first characterizing fluid flow across the devices actuated at physiologically relevant frequencies and pressures, which mimic physiological heart rates and blood pressures, respectively. We aim to shift our focus towards 2-layer devices (without the top actuation layer), through which flow can be driven by the arterial pulse on the human wrist.

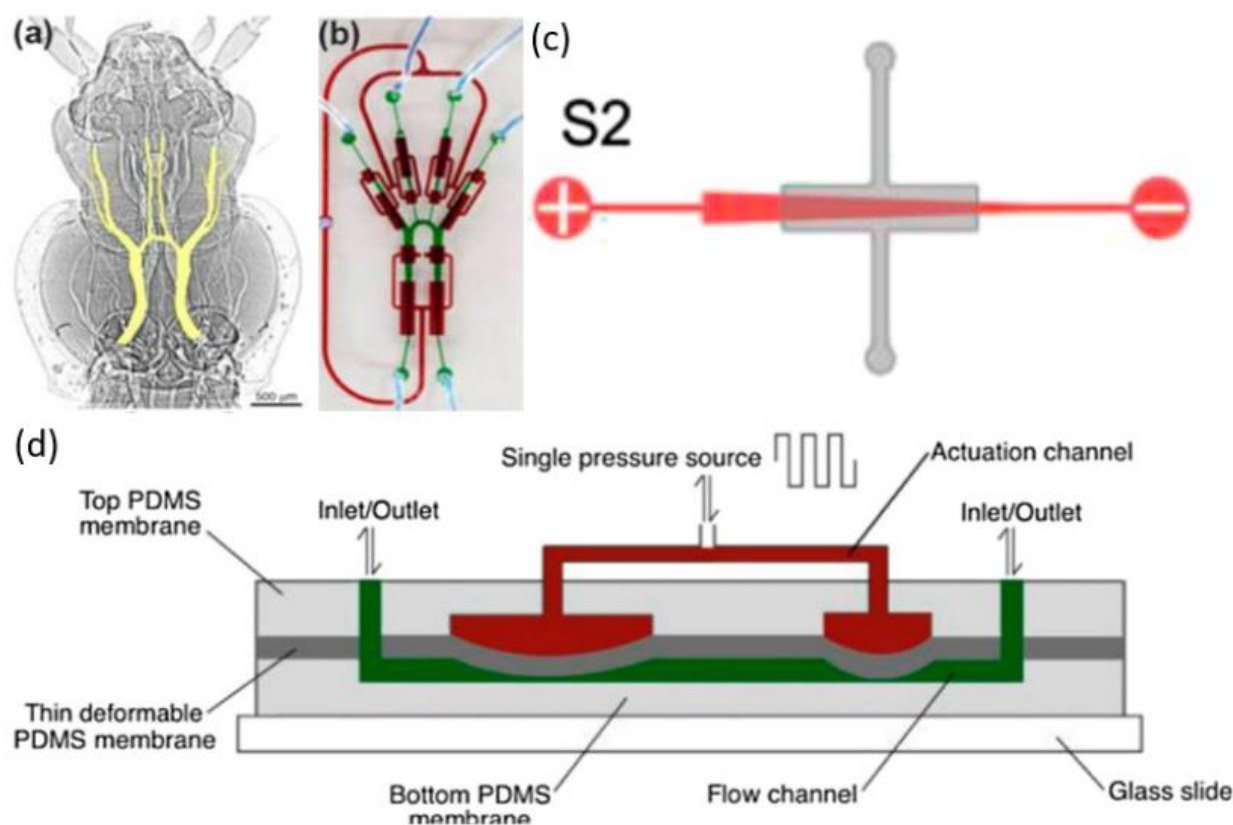


**Figure 1.1. Insect respiratory system and insect-mimetic microfluidic devices.**<sup>33</sup> (a) An X-ray image of the tracheal tubes in the beetle *Platynus decentis*, with the main tracheal tubes highlighted in yellow. (b) A multichannel microfluidic device that mimics the design of main respiratory channels of an insect. (c) A single-channel insect-mimetic microfluidic device, with the fluid flow channel shown in red and the actuation (pressurized air) channel shown in gray. (d) A detailed view of a 3-layer insect-mimetic microfluidic device. Republished with permission of IOP Publishing Ltd., from “Frequency-specific, valveless flow control in insect-mimetic microfluidic devices” by K. Chatterjee, P. M. Graybill, J. Socha, R. V. Davalos, and A. Staples, *Bioinspiration & Biomimetics*, Vol. 16, No. 3, © 2021 IOP Publishing Ltd; permission conveyed through Copyright Clearance Center, Inc.

The skin is known for its impermeability for substances, so there have been many methods in disrupting the skin for drug delivery, including the use of electroporation, chemical treatment, thermal treatment, mechanical abrasion, and the use of microneedle arrays.<sup>36-44</sup> Hollow microneedle arrays are especially advantageous over the other methods because they can deliver drugs and penetrate the skin simultaneously. Yeung and colleagues (2019) developed microneedle arrays with syringe-shaped microneedles for efficient penetration.<sup>45</sup> For insulin delivery, however, longer and sharper microneedles are needed to penetrate into the dermis, so we have redesigned the microneedle arrays using COMSOL Multiphysics for enhanced insulin delivery.<sup>46-48</sup> We have also added a closed, cuboidal “reservoir” structure with a cylindrical inlet to the bottom of the microneedle array (Figures 3.3-3.5), so that it can form a closed system with the microfluidic pump for fluid flow.<sup>49</sup>

In this study, we have fabricated functional microfluidic devices (pumps) as well as functional microneedle arrays. We performed extensive testing on several microfluidic devices with the general channel design S2 in Chatterjee et al. (2021) (Figure 1.1c),<sup>33</sup> to characterize the flow rate across each device at a range of physiologically relevant actuation frequencies and pressures. We also have tested the penetration performance of microneedle arrays using porcine skin samples and determined the microneedle array with an optimal performance. Finally, we have assembled the microfluidic pump and the microneedle array into wearable, integrated patch-pump prototypes.

This article is structured as follows. Chapter 2 provides the materials and methods used for the fabrication and testing of the devices and microneedle arrays. Key results are collected in Chapter 3. Discussion of the results and limitations of the study is presented in Chapter 4, and final conclusions of the study as well as future directions are covered in Chapter 5.

# Chapter 2

## Materials and Methods

### 2.1 Fabrication of Microfluidic Pump

#### 2.1.1 Master mold fabrication

Master molds were fabricated using photolithography with a SU-8 negative photoresist on a silicon wafer, following protocols provided by Microchem.<sup>50</sup> A silicon wafer with a diameter of 100 mm and thickness of 525  $\mu\text{m}$  (WaferPro, ID2303) was cleaned by spraying acetone followed by 91% isopropyl alcohol. The wafer was then baked on a hot plate (Torrey Pines Scientific) at 120  $^{\circ}\text{C}$  for 15 minutes and then slowly cooled down to a temperature of 65  $^{\circ}\text{C}$ . The wafer was placed into the center of a spin coater (Laurell Technologies Corporation, Model WS-650Mz-23NPPB), which was connected to a vacuum pump and a clean, dry pressurized air source for operation. Approximately 5 mL of SU-8 2075 (Microchem #Y111074) was poured onto the center of the wafer, and the spin coater was programmed to spin at 500 rpm for 10 seconds, accelerated to a higher speed depending on the target SU-8 layer thickness, and spun for 30 seconds. To achieve a layer thickness of 80  $\mu\text{m}$ , a spin speed of 2700 rpm was used. The wafer was immediately placed onto the hot plate for soft baking at 65  $^{\circ}\text{C}$  and then 95  $^{\circ}\text{C}$  for a specified amount of time depending on the SU-8 layer thickness. For an 80- $\mu\text{m}$ -thick layer, the baking time was 3 minutes at 65  $^{\circ}\text{C}$  and 9 minutes at 95  $^{\circ}\text{C}$ . After the soft bake, the wafer was slowly cooled to room temperature on the hot plate. At room temperature, the wafer was placed into a UV lamp (UV-KUB 2), and a glass slide and then a photomask for the channel pattern based on design S2 from Chatterjee et al. (Figure 1.1c) were placed on top of the wafer.<sup>33</sup> After the UV exposure, the wafer was placed onto the hot plate for a post-exposure baking step, at 65  $^{\circ}\text{C}$  and then 95  $^{\circ}\text{C}$  for a specified amount of time depending on the target layer thickness. For a layer thickness of 80  $\mu\text{m}$ , the baking time was 2 minutes at 65  $^{\circ}\text{C}$  and 7 minutes at 95  $^{\circ}\text{C}$ . The wafer was again cooled down to room temperature and stayed covered overnight. On the next day, development was done by placing the wafer into 80 mL of propylene glycol methyl ether acetate (PGMEA, Kayaku Advanced Materials) and manually agitating for a specified amount of time. The development time was specified to be 7 minutes for an 80- $\mu\text{m}$ -thick layer. The wafer was then dried with pressurized air and baked on the hot plate at 150  $^{\circ}\text{C}$  for 20 minutes. All heating steps were performed at a rate of 7.5  $^{\circ}\text{C}/\text{min}$ , and all cooling steps were performed at a rate of 5.0  $^{\circ}\text{C}/\text{min}$ .

#### 2.1.2 PDMS device fabrication

To make the top (actuation) and bottom (flow) layers of the microfluidic pump, approximately 30 mL of polydimethylsiloxane (PDMS; SYLGARD™ 184 Silicone Elastomer Base, Dow

Chemical Company) base was mixed with 3 mL of the curing agent (SYLGARD™ 184 Silicone Elastomer Curing Agent, Dow Chemical Company) for each layer. The mixture was stirred and then degassed for 30 minutes. After degassing, the PDMS mixture was poured over a master mold of the corresponding layer and baked in an oven at 90 °C for 2 hours. After baking, each layer was manually peeled off from the master mold, cut according to the alignment marks into smaller rectangular “device layers.” Using a biopsy punch with a diameter of 0.75 mm (Robbins Instruments, RBP-075P), a hole was punched at the inlet/outlet of each top device layer and at both the inlet and the outlet of each bottom device layer. The middle layer (elastomeric membrane) of the device was made by spinning a very thin (20 µm) layer of PDMS-curing agent mixture onto a silicon wafer. Specifically, a silicon wafer identical to one used to make master molds was silanized by placing into a Petri dish, adding a few drops of trimethylchlorosilane (TMCS, Thermo Fisher Scientific), sealing the Petri dish with Parafilm (Bemis), and incubating for 2 hours. After silanization, the wafer was placed into the center of the spin coater, cleaned using isopropyl alcohol, and spin-dried at 4000 rpm for 60 seconds. Approximately 6 g of PDMS-curing agent mixture (mixing ratio 5:1) was then poured onto the center of the wafer. The spin coater was programmed to spin at 500 rpm for 10 seconds and 4000 rpm for 60 seconds. After spinning, the wafer was baked in the oven at 90 °C for 45 minutes. After the wafer was cooled down to room temperature, the bottom device layers were bonded to the membrane by treating the surfaces with plasma using the plasma cleaner (Harrick Plasma, PDC-001) at 0.5 mmHg for 1 minute and gently dropping the bottom device layer onto the wafer. The wafer was then baked at 90 °C for 30 minutes and left overnight at room temperature to enhance bonding. On the next day, the bottom device layers together with the membrane were manually peeled off from the wafer. The middle-bottom combined device layer was then plasma bonded to the top device layer. After the surfaces were plasma treated at 0.5 mmHg for 1 minute, the device layers were gently aligned together using the alignment marks. The devices were then baked at 90 °C for 30 minutes and left overnight to reinforce bonding.

### **2.1.3 Alternative method of device fabrication**

An alternative method of fabricating the microfluidic device was 3D printing the device using a Form 2 or Form 3 printer (Formlabs). The device geometry was designed using COMSOL Multiphysics® 5.6, exported as an STL file into PreForm 3.23.1, a graphic user interface for Formlabs printers. Using the PreForm software, the geometry was tilted to an angle to reduce the suction force on the printer platform, and supports were added to the structure. The device was then printed using Elastic 50A resin (Formlabs, RS-F2-ELCL-01) with the printer.

## **2.2 Fabrication of Microneedle Array**

Hollow microneedle arrays were fabricated using 3D printing with a Form 3 or Form 2 printer (Formlabs). Microneedle array prototype geometries were designed with COMSOL Multiphysics®, and each prototype was exported as an STL file into the PreForm software.

Using the PreForm software, the geometry was tilted to an angle to reduce the suction force on the printer platform, and supports were added to the structure. The microneedle array was then printed using the printer.

Resins used to print the microneedle arrays included Surgical Guide (Formlabs, RS-F2-SGAM-01), Clear (Formlabs, RS-F2-GPCL-04), Rigid 4000 (Formlabs, RS-F2-RGWH-01), and Tough 2000 (Formlabs, RS-F2-TO20-01). Microneedle arrays made of Surgical Guide resin were printed using a Form 2 printer, while the rest of microneedle arrays were printed using a Form 3 printer. Washing and curing protocols were dependent on the specific resin used.

## **2.3 Penetration Testing of Microneedle Arrays**

Microneedle arrays of different geometries made of different printing resins were tested using porcine skin samples purchased from a local butcher shop. A syringe pump (New Era, Model NE-300) was used to deliver dyed water at a flow rate of 5.1 mL/hr into the microneedle array, which was manually pressed in porcine skin, for two minutes. The excessive dye on the superficial surface of the skin was blotted, and the skin was cut at three locations perforated by the microneedle array. The depth at which the dye had penetrated was measured using a caliper at three locations of the penetrated skin area. The mean and standard deviation in the penetration depth of each microneedle array was calculated and plotted.

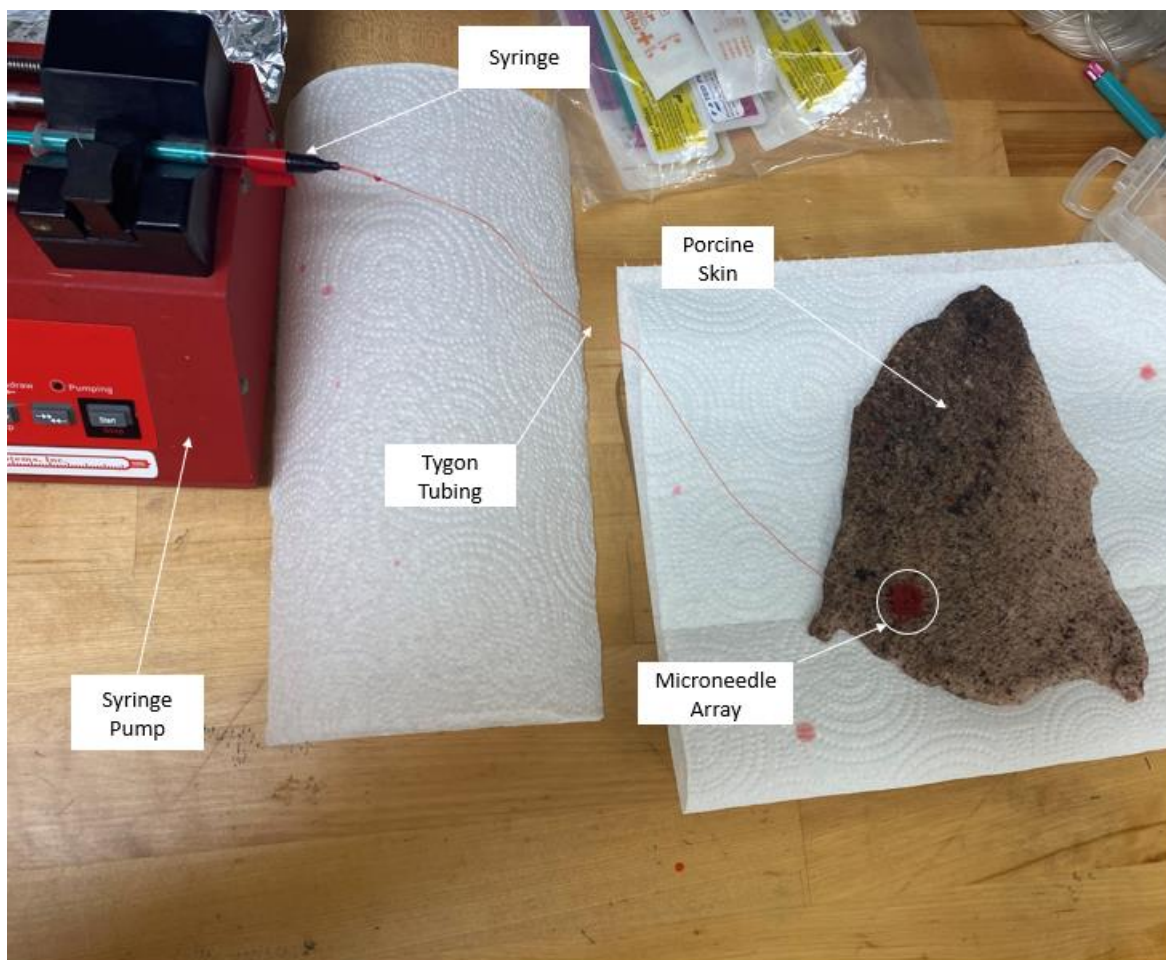


**Figure 2.1: Microneedle Array Penetration Testing Apparatus.** A syringe pump was used to deliver dyed water through a syringe and a piece of Tygon tubing to a 3D-printed microneedle array embedded in porcine skin.

## 2.4 *Ex Vivo* Flow Testing of Microfluidic Devices

### 2.4.1 Flow Testing Procedure

For flow testing, a microfluidic device (pump) was placed into the slot cut from a thin piece of wood, with the bottom device layer facing up (shown in Figure 2.2). A 10-cm-long piece of Tygon tubing with a diameter of 0.75 mm was attached to each of the inlet and the outlet of the microfluidic pump through the punched holes on the bottom device layer. Each of the two pieces of tubing was taped against the wood to minimize the effect of gravity. The device and the pieces of Tygon tubing were filled with dyed water using a 1 mL syringe. The combined inlet/outlet of the actuation layer was connected to an apparatus used to generate a square wave of pressurized air through a 3-cm-long piece of Tygon tubing with a diameter of 0.75 mm. The apparatus (Figure 2.2) was composed of a tunable pressurized air line on the laboratory wall, a vacuum pump (Platinum, Serial No. 0511), a DC power supply (BK Precision, Model 1623A), an

Arduino Uno microcontroller, a control board (Arduino), a pressure regulator (ControlAir, Inc., Type 90), and a solenoid valve (Festo, MHE2-MS1H-5/2-QS-4-K). To start the testing, a laptop was connected to the Arduino that was connected to the DC power supply. The voltage and current on the DC power supply were adjusted to 12.0 V and 1.0 A, respectively. A simple “blink” Arduino program was run, and the Arduino should start making a periodic clicking sound with a blinking green light. The switch for the air line was gently turned on by tapping with a wrench, until the barometer reading started to oscillate between 0 and 0.5 bar. The pressure controller was also adjusted so that the barometer on the pressure controller had a reading between 0 and the desired pressure for testing. The vacuum pump was then connected to the solenoid valve (as shown in Figure 2.2). A 30-cm ruler was placed on the wood in such a way that the 16-cm and 20-cm marks on the ruler lined up with the respective marks on the wood (Figure 2.2). To start the flow, the vacuum pump was turned on, and a video recording was started. The video recording was stopped before the liquid-air interface reached the device.

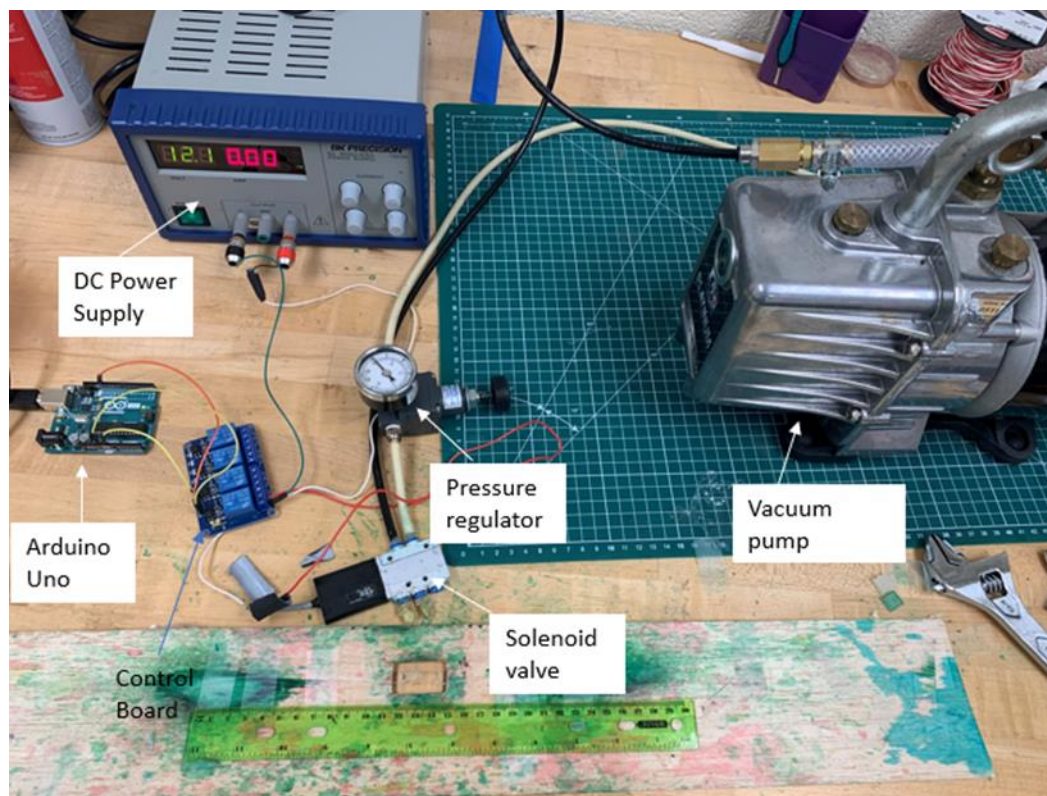


**Figure 2.2: The flow testing apparatus with pressurized air.** A simple blink program on the Arduino Uno was used to control the pressurized air through the solenoid valve, which periodically switched between the pressurized air inlet and the vacuum inlet, forming a square wave in air pressure. The pressurized air, along with the air line on the wall, controlled the magnitude of the air pressure. The vacuum pump was used to re-expand the membrane to the original state after its collapse against the flow channel floor induced by the pressurized air.

## 2.4.2 Data Analysis

For data analysis, each video recording was replayed, and a stopwatch was used to time the flow over an approximately 4-cm interval. Specifically, when the air-water interface at the inlet (in the video) was approximately 6 cm away from the nearest edge of the device on the inlet side, the video was paused, and the position of the air-water interface along the ruler was recorded. The video and the stopwatch were started simultaneously at this point, and they were then stopped simultaneously when the air-water interface was approximately 2 cm away from the nearest edge of the device. An Excel datasheet was made to record all the data, including flow channel width, tubing cross-sectional area, actuation frequency, actuation pressure, as well as the distance travelled by the air-water interface and the time taken. The flow rate was then calculated from the time taken, the distance travelled, and the tubing cross-sectional area. Since the flow was driven by shear forces due to the collapse of the membrane, there is no definitive formula used to calculate the hydraulic resistance. Instead, we can estimate the hydraulic resistance using the actuation pressure, assuming the actuation pressure is roughly balanced with the shear force that drives the flow. From the flow rate, the hydraulic resistance of the system was estimated using the formula below:<sup>51</sup>

$$R_H = \frac{P_{act}}{Q} \quad (2.1)$$

Where,  $R_H$  is the hydraulic resistance,  $P_{act}$  is the actuation pressure, and  $Q$  is the flow rate.

## 2.4.3 Flow Testing Experiments

### 2.4.3.1 Preliminary testing of multiple devices at three physiologically relevant actuation pressures and frequencies.

Each microfluidic device was first tested as described above under three physiologically relevant actuation pressures (approximately 100, 150, and 200 mmHg) at a constant actuation frequency of 60 bpm. The microfluidic devices were then tested under three physiologically relevant actuation frequencies (60, 90, and 120 bpm) under a constant actuation pressure of 100 mmHg. The flow rate across each device was plotted against the actuation frequency and actuation pressure.

### 2.4.3.2 Generation of a flow rate profile of model device across a range of physiologically relevant actuation frequencies and pressures.

A model device was chosen based on the highest consistency of flow performance to generate a more complete flow rate profile over a wider range of actuation frequencies and pressures. The model device was tested at 12 physiologically relevant actuation frequencies (30, 45, 60, 72, 84, 96, 108, 120, 135, 150, 165, and 180 bpm) under a constant actuation pressure of 100 mmHg, and then tested under 7 physiologically relevant actuation pressures (75, 94, 113, 131, 150, 188, and 225 mmHg) at a constant actuation frequency of 60 bpm and then 90 bpm. The flow rate was plotted against the actuation frequency and actuation pressure.

#### 2.4.3.3 Investigation of the effect of additional components on flow rate and hydraulic resistance.

After testing with no additional component attached to the outlet, a  $5 \times 5$  microneedle array made of Surgical Guide Resin was attached to the Tygon tubing at the outlet, and testing was performed at a constant actuation pressure of 100 mmHg and 9 physiologically relevant actuation frequencies (30, 45, 60, 72, 84, 96, 108, 120, and 135 bpm). Subsequently, the microneedle array was embedded in a piece of porcine skin and attached to the outlet Tygon tubing, and the experiment was repeated. The flow rate was plotted against the actuation frequency for each of three experimental conditions. The total hydraulic resistance of the system was estimated using Equation 2.1 and plotted against the actuation frequency for each experimental condition.

#### 2.4.3.4 Detailed testing of more devices and characterization of flow rate as a function of multiple variables.

Four other devices with flow channel widths different from the model device were also tested under the same 12 actuation frequencies (at a constant actuation pressure of 100 mmHg) and 7 actuation pressures (at a constant actuation frequency of 60 bpm) as described in section 2.4.3.2. The flow rate was then measured as mentioned above and plotted against the actuation frequency and actuation pressure for each device. The data were then rearranged so that the flow rate was plotted against the flow channel width at each actuation frequency and each actuation pressure.

## 2.5 Assembly of Components into a Wearable Patch-Pump

The outlet (“+” end) of a microfluidic device and the inlet of a microneedle array were connected using a short piece of Tygon tubing of a diameter of 0.75 mm. A thin piece of adhesive was also applied to hold the two components together. Alternatively, a casing designed to fit the microneedle array, the microfluidic device, and the Tygon tubing was designed using SOLIDWORKS CAD software and 3D-printed using Surgical Guide resin (Formlabs). The microneedle array and the microfluidic device connected with the Tygon tubing were carefully placed into the casing.

## 2.6 Statistical Analysis

Statistical analysis was conducted with the GraphPad Prism 9 software. A one-way ANOVA was performed to assess differences in flow rate and hydraulic resistance across the three experimental groups (no microneedle array, with microneedle array, and with microneedle array in porcine skin) as described in section 2.4.3.3. A simple linear regression model was generated to correlate the flow rate and the actuation frequency and pressure for each of the five devices characterized in detail as described in sections 2.4.3.2 and 2.4.3.4. The data were then replotted to correlate the flow rate with the flow channel width at each actuation frequency and pressure.

An F-test was used to examine the statistical significance of the slope in each condition. A significance level of  $\alpha = 0.05$  was used in all tests.

# Chapter 3

## Results

### 3.1 Fabrication of Patch-Pump

#### 3.1.1 Master Mold Fabrication

Using standard photolithography techniques described in section 2.1.1, a master mold can be created by depositing channel patterns on a silicon wafer as shown in Figure 3.1. Each master mold is designed to make 15 devices for each batch with five different flow channel widths as listed in Table 3.1 and can be used repeatedly.

**Table 3.1:** Flow channel widths of devices produced by the current photomask/master mold system. All devices have a flow channel length of 11200  $\mu\text{m}$  at the converging (triangular) region, and the thickness of the SU-8 layer (channel depth) was dependent on the spinning speed while depositing the layer. Device numbers are shown on the master mold for the bottom layer in Figure 3.1b, and all device numbers mentioned in this report section follow the numbering convention mentioned in this table. The depth was 80  $\mu\text{m}$  for actuation and flow channels of all devices used in this study.

Device number	Flow channel width ( $\mu\text{m}$ )
1	4600
2	2300
3	4600
4	2300
5	4600
6	4025
7	2875
8	4025
9	3450
10	3450
11	3450
12	2875
13	2875
14	2300
15	4025

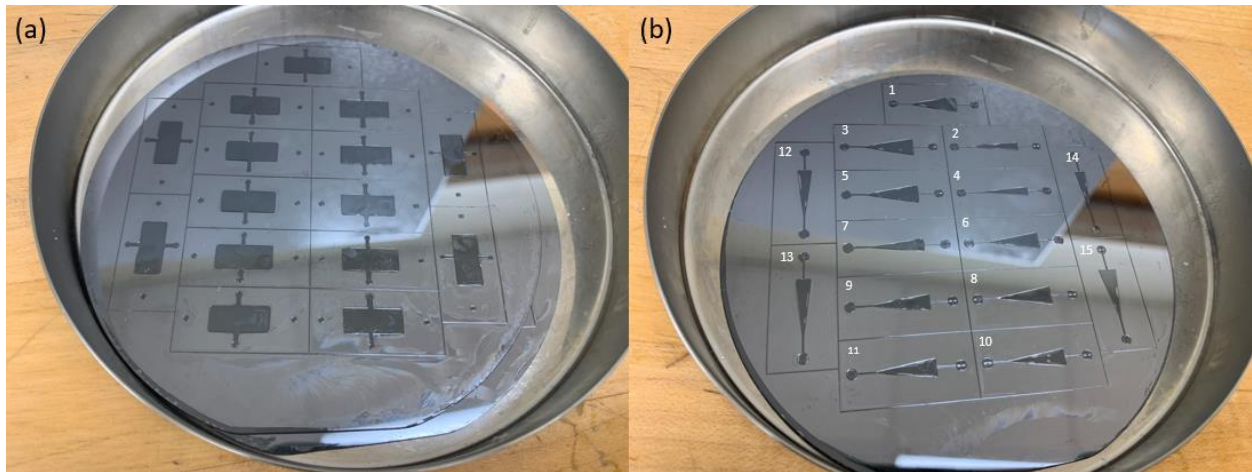


**Figure 3.1: Master molds fabricated using photolithography.** The negative channel designs were achieved using photomasks that enabled selective curing of SU-8 under the UV light. (a) Master mold for top layer with 15 identical actuation channel patterns, and (b) mold for bottom layer with 5 different flow channel designs, each with 3 replicates.

### 3.1.2 Microfluidic device fabrication

Using replica molding and plasma bonding techniques as described in section 2.1.2, microfluidic pumps were fabricated as shown in Figure 3.2b. A batch of 15 microfluidic devices with five different flow channel widths, as shown in Table 3.1, could be fabricated from each pair of master molds. Using square waves of pressurized air, the flow was driven toward the outlet through periodic contractions as shown in Figure 3.2c-d. Figure 3.2a shows a microfluidic pump geometry we created by COMSOL Multiphysics®, which could be used to print the devices using 3D printing as an alternative method described in section 2.1.3. However, due to the fine resolution required for the devices, the 3D printing method proved to be impractical.

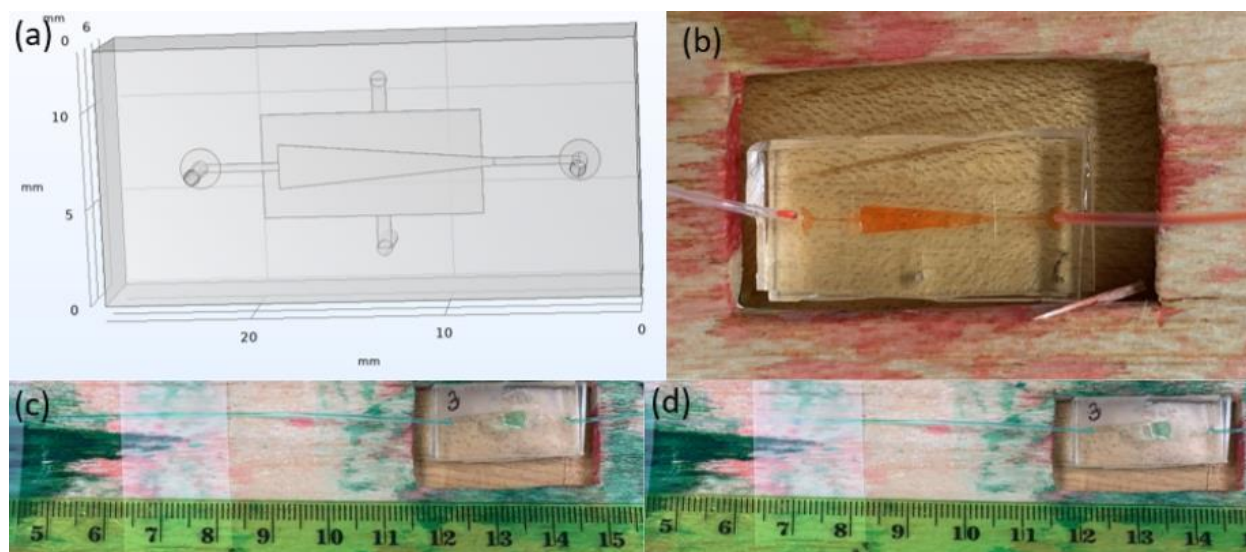


**Figure 3.2: Microfluidic pump design and operation.** (a) Microfluidic pump geometry constructed with COMSOL Multiphysics. (b) A working microfluidic device with the flow channel filled with red dyed water. Parts (c) and (d) show a microfluidic pump (flow channel width =  $4600\ \mu\text{m}$ ) during flow testing, where (c) is taken at time  $t = 0$ , and (d) is taken at time  $t = 10$  seconds. Note how the position of the air-water interface at the inlet changed over time.

### 3.1.3 Microneedle array fabrication

The syringe-shaped microneedle array design is based on Yeung et al. (2019) (Figure 3.3a).<sup>45</sup> To adapt for the transdermal delivery of insulin, a series of different microneedle array prototypes were designed in COMSOL Multiphysics and printed using a Formlabs 3D printer via the PreForm interface (as described in section 2.2). We have designed and printed six successful microneedle array prototypes on the top surface of a cuboidal reservoir structure, with CAD geometries shown in Figure 3.4 and main dimensions shown in Table 3.2. Figure 3.3b-d shows our optimal microneedle array design for transdermal fluid delivery ( $5 \times 5$  design 2 made of Surgical Guide resin), which was determined by penetration testing described in section 3.2.

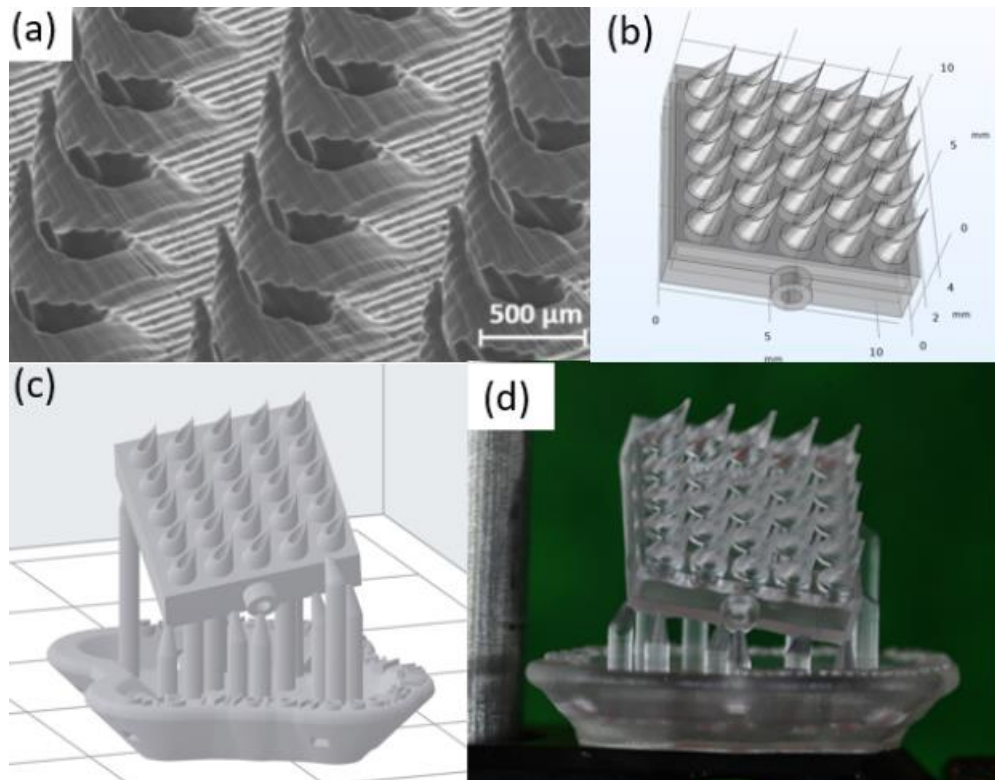


**Figure 3.3: 3D printed microneedle arrays.** (a) A syringe-shaped, 3D-printed microneedle array prototype developed by Yeung et al. (2019).<sup>45</sup> “A 3D-printed microfluidic-enabled hollow microneedle architecture for transdermal drug delivery” by C. Yeung, S. Chen, B. King, H. Lin, K. King, F. Akhtar, G. Diaz, B. Wang, J. Zhu and W. Sun is licensed under CC BY 4.0. (b) A  $5 \times 5$  microneedle array prototype developed by COMSOL Multiphysics adapted for insulin delivery ( $5 \times 5$  design 2). (c) The microneedle array prototype in part (b) imported and modified in PreForm. (d) A 3D printed microneedle array in Clear Resin (Formlabs, RS-F2-GPCL-04).

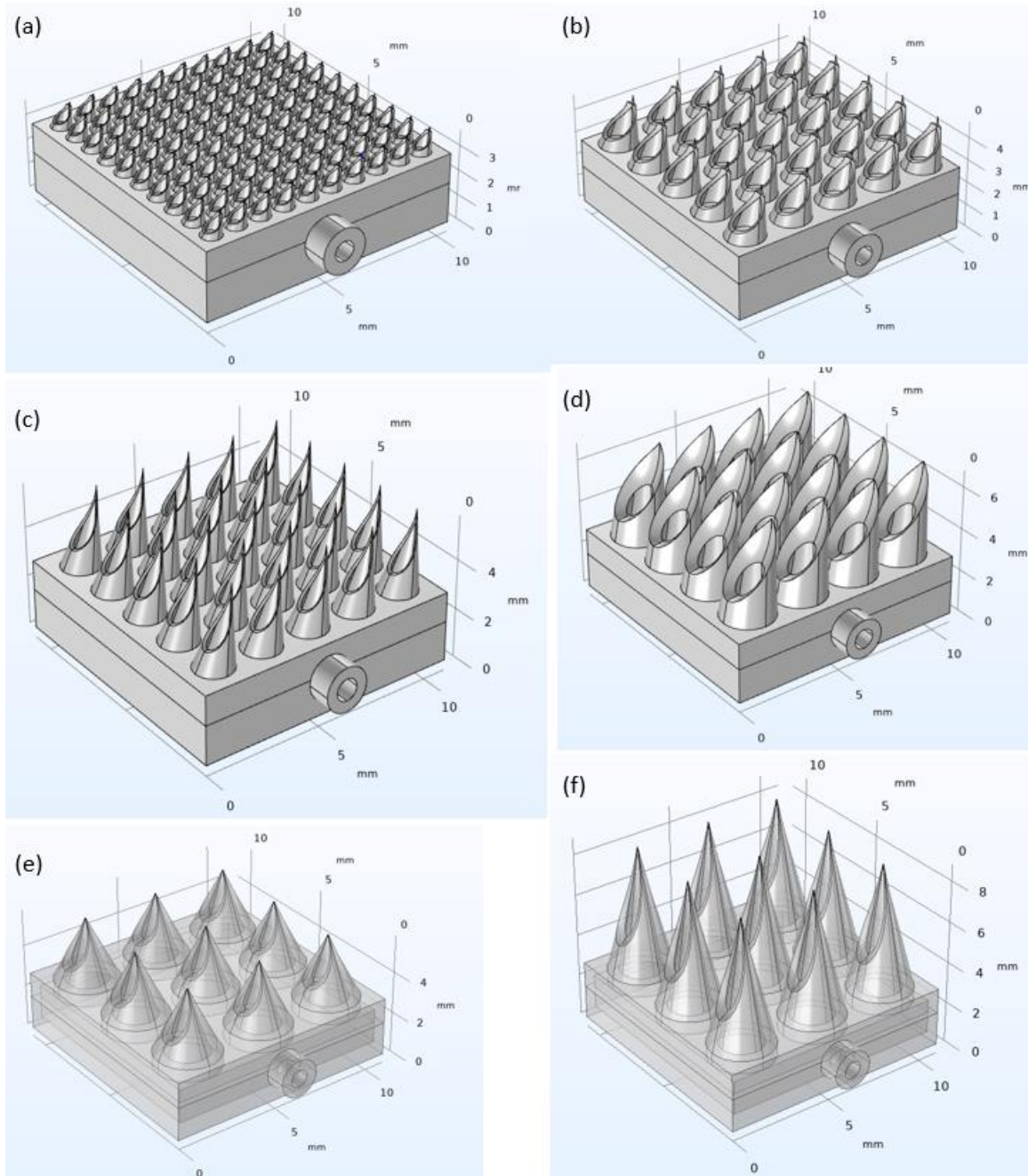


**Figure 3.4: CAD prototypes of six microfluidic designs adapted for transdermal insulin delivery developed using COMSOL Multiphysics. (a)  $10 \times 10$  design 1, (b)  $5 \times 5$  design 1, (c)  $5 \times 5$  design 2, (d)  $4 \times 4$  design 1, (e)  $3 \times 3$  design 1, and (f)  $3 \times 3$  design 2.**

**Table 3.2: Shapes and dimensions of the six microneedle array prototypes.**

Microneedle Array Design	Microneedle Shape	Base Width (mm)	Base Depth (mm)	Needle Outer Radius (mm)	Needle Bore Radius (mm)	Total Needle Length (mm)
10 × 10 Design 1	Eccentric cone with syringe-shaped opening; blunt top with thin cylindrical element	11.0	11.0	0.4	0.3	0.8
5 × 5 Design 1	Eccentric cone with syringe-shaped opening; blunt top with thin cylindrical element	11.0	11.0	0.8	0.6	1.9
5 × 5 Design 2	Eccentric cone with syringe-shaped opening; pointed top	11.0	11.0	0.8	0.6	3.0
4 × 4 Design 1	Eccentric cone cut by ellipsoid; blunt top	11.0	11.0	1.2	0.7	4.0
3 × 3 Design 1	Cone with syringe-shaped opening; pointed top	11.0	11.0	1.5	1.0	3.0
3 × 3 Design 2	Cone with syringe-shaped opening; pointed top	11.0	11.0	1.5	1.0	6.0

## 3.2 Penetration Testing of Microneedle Arrays

Nine different 3D-printed microneedle array prototypes were tested for the depth of penetration through a piece of porcine skin (Figure 3.5). Information for the microneedle array prototypes, along with the testing results, are shown in Table 3.3.

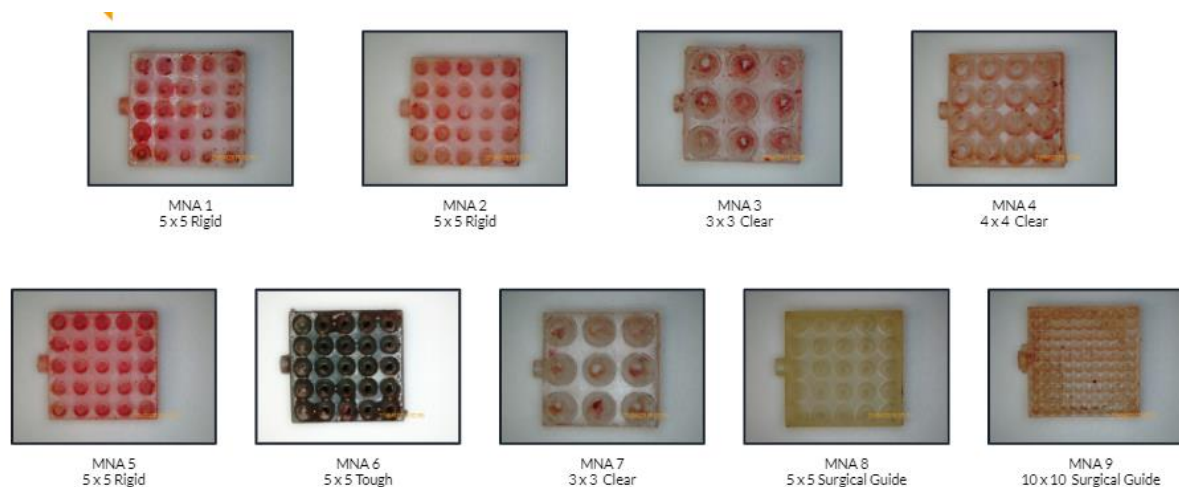


**Figure 3.5: Microneedle array prototypes involved in the porcine skin penetration testing.**

Nine microneedle arrays of six microneedle designs (please refer to Figure 3.4) and four different Formlabs resins (Clear, Rigid 4000, Tough 2000, and Surgical Guide) were used.  
(Photography and figure design: Jenna Sims)

Each microneedle array was pressed against a piece of porcine skin, and a syringe pump (New Era, Model NE-300) was used to drive the flow of dyed water at a constant rate of 5.1 mL/hr for two minutes (as described in Section 2.3). The penetration depth was measured using a caliper at three locations, and the average and standard deviation of the penetration depth by each microneedle array is shown in Table 3.3 and Figure 3.6.

**Table 3.3: Penetration testing data of microneedle array prototypes against porcine skin**  
(please refer to Figure 3.4 for the six microneedle array designs).

Microneedle array number	Resin	Design	Punctured Skin?	Location 1 Depth (mm)	Location 2 Depth (mm)	Location 3 Depth (mm)	Average Depth (mm)	Standard Deviation (mm)
1	Rigid	5 x 5 (Design 2)	Yes	0.6	0.5	0.5	0.533	0.058
2	Rigid	5 x 5 (Design 1)	Yes	0.4	0.7	0.5	0.533	0.153
3	Clear	3 x 3 (Design 2)	Yes	0.8	0	0	0.267	0.462
4	Clear	4 x 4	Yes	0.4	0.2	1.2	0.6	0.529
5	Rigid	5 x 5 (Design 2)	Yes	0.9	0.6	0.8	0.267	0.153
6	Tough	5 x 5 (Design 2)	Yes	0.1	0.1	0.5	0.233	0.231
7	Clear	3 x 3 (Design 1)	Yes	0	0	0	0	0
8	Surgical Guide	5 x 5 (Design 2)	Yes	1.6	1.3	1.4	1.433	0.153
9	Surgical Guide	10 x 10	Yes	1.4	0.6	1.2	1.067	0.417

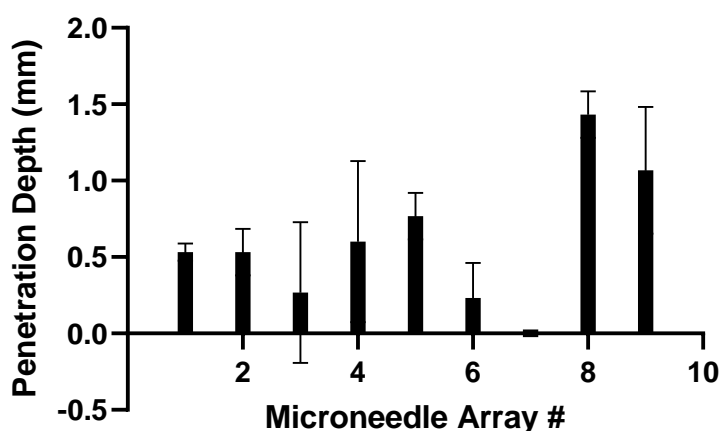


**Figure 3.6: Penetration testing data of nine microneedle arrays.** The experiment was conducted as described in Section 2.4, and the depth at which the dye penetrated through the porcine skin was measured at three locations with a caliper. The average penetration depth was plotted for each microneedle array.

Out of the nine microneedle arrays, we found that microneedle array #8, which was the sharpened, lengthened  $5 \times 5$  prototype (design 2) made of Surgical Guide resin, showed the highest penetration depth and a very high uniformity of penetration at different locations of the porcine skin. For this microneedle array prototype, the microneedles were able to penetrate through the porcine skin with an average penetration depth of 1.43 mm and a standard deviation of 0.15 mm.

### 3.3 *Ex Vivo* Flow Testing of Microfluidic Devices

#### 3.3.1 Preliminary characterization of flow rate across a series of microfluidic pumps at three actuation frequencies and pressures.

A series of six working microfluidic pumps with a flow channel depth of  $80 \mu\text{m}$  and an elastomeric membrane thickness of  $20 \mu\text{m}$  were tested under pressurized air under a constant actuation frequency of 60 bpm, which roughly matched the physiological resting heart rate, and three different actuation pressures (100, 150, and 200 mmHg, representing normal, moderately hypertensive, and severely hypertensive systolic blood pressures, respectively).<sup>52-56</sup> The flow channel widths of the six devices were listed in Table 3.1. The flow rate was measured as described in section 2.4, and five replicates were done on each experimental condition for each device. Data were plotted in Figure 3.7a.

Three of the six devices were then tested under pressurized air under a constant actuation pressure of 100 mmHg and at three different actuation frequencies (60, 120, and 180 bpm, representing heart rate at rest, during moderate exercise, and during very vigorous exercise,

respectively).<sup>57,58</sup> The flow rate was measured as described in section 2.4, and five replicates were done on each experimental condition for each device. Data were plotted in Figure 3.7b.

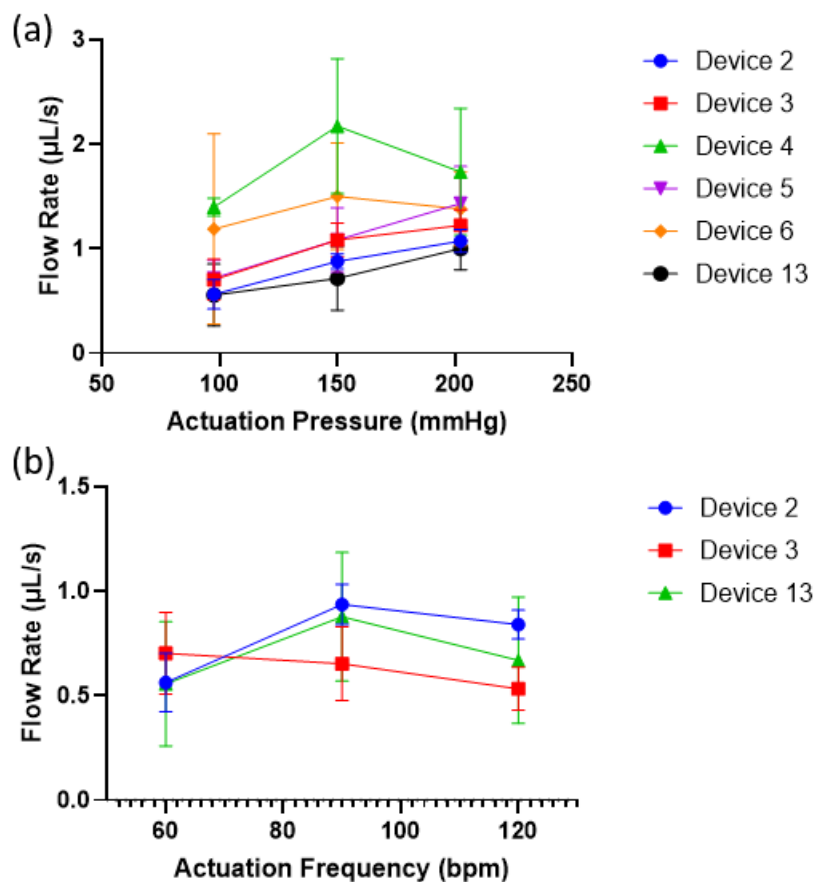


**Figure 3.7: Characterization of flow rate across a series of microfluidic devices against actuation pressure and frequency.** (a) Plot of flow rate against actuation pressure for a series of six devices actuated under pressures of 100, 150, and 200 mmHg and at a constant frequency of 60 bpm. (b) Plot of flow rate against actuation frequency for a series of three devices actuated at frequencies of 60, 90, and 120 bpm and under a constant pressure of 100 mmHg. All devices had a flow channel depth of  $80\ \mu\text{m}$ , and the flow channel widths are described in Table 3.1.

### 3.3.2 Flow rate profile of a narrow-flow-channel model device across a spectrum of actuation pressures and frequencies.

A model device was selected based on the minimal variance under each experimental condition. The model device (device #2 in Table 3.1) had a flow channel width of  $2300\ \mu\text{m}$ , which was the narrowest flow channel width of all devices tested. The model device was then tested at nine different actuation frequencies between 30 and 180 bpm under a constant actuation pressure of 100 mmHg. The experiment was then repeated, with two additional data points added (135 and

165 bpm). The device was then tested under seven different actuation pressures between 75 and 225 mmHg at a constant actuation frequency of 60 bpm, and then the experiment was repeated at 90 bpm. The flow rate was measured as described in section 2.4, and five replicates were done on each experimental condition per trial.

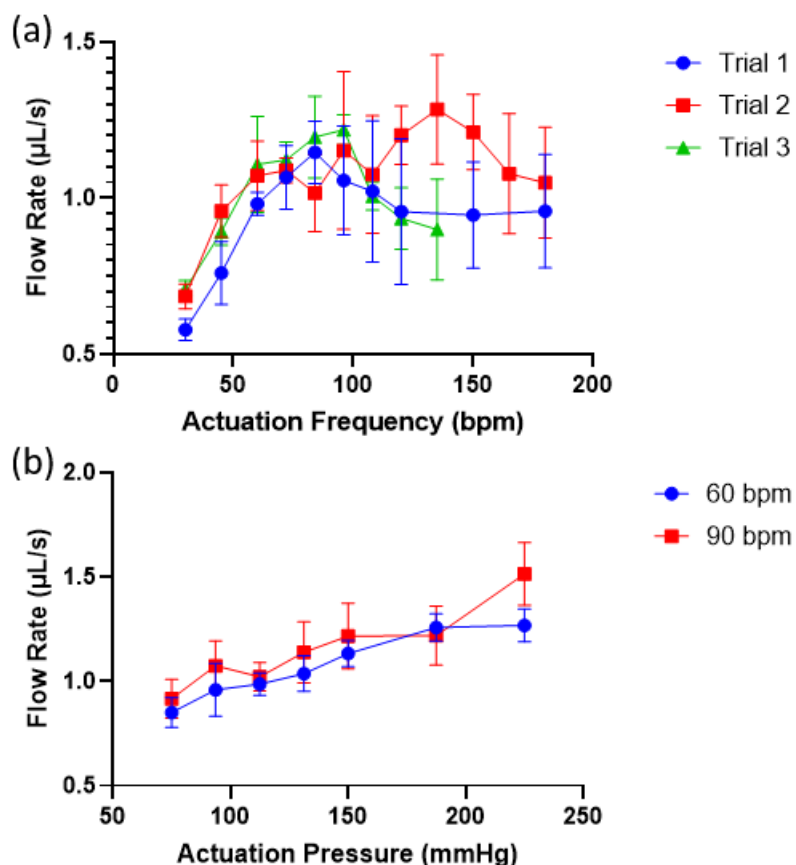


**Figure 3.8: Detailed characterization of flow rate across the model device (device #2, flow channel width 2300  $\mu\text{m}$ , depth 80  $\mu\text{m}$ ).** (a) Plot of flow rate against actuation frequency at actuation frequencies between 30 and 180 bpm and a constant pressure of 100 mmHg. (b) Plot of flow rate against actuation pressure at seven actuation pressures between 75 and 225 mmHg and a constant frequency of 60 and 90 bpm.

### 3.3.3 Flow rate profile of a narrow-flow-channel model device with additional components added.

To investigate the effect of the microneedle array and the porcine skin on the overall flow rate and hydraulic resistance, we measured the flow rate across the model device with no microneedle array attached (as a control), with a microneedle array attached to the outlet, and with a microneedle array embedded in porcine skin attached to the outlet. This experiment was performed at nine different actuation frequencies from 30 to 135 bpm, and five replicates were

done on each combination of experimental conditions per trial. Data were plotted in Figure 3.9. Similar to the trials shown in Figure 3.8a, the flow rate first increased and then decreased with increasing actuation frequency regardless of the addition of the microneedle array and the porcine skin. In addition, we have found no significant difference in the flow rate or the total hydraulic resistance caused by the microneedle array and porcine skin (a one-way ANOVA shows that  $p > 0.1$  at all actuation frequencies), so subsequent *ex vivo* flow testing (as shown in Figure 3.10-13) did not involve these components.

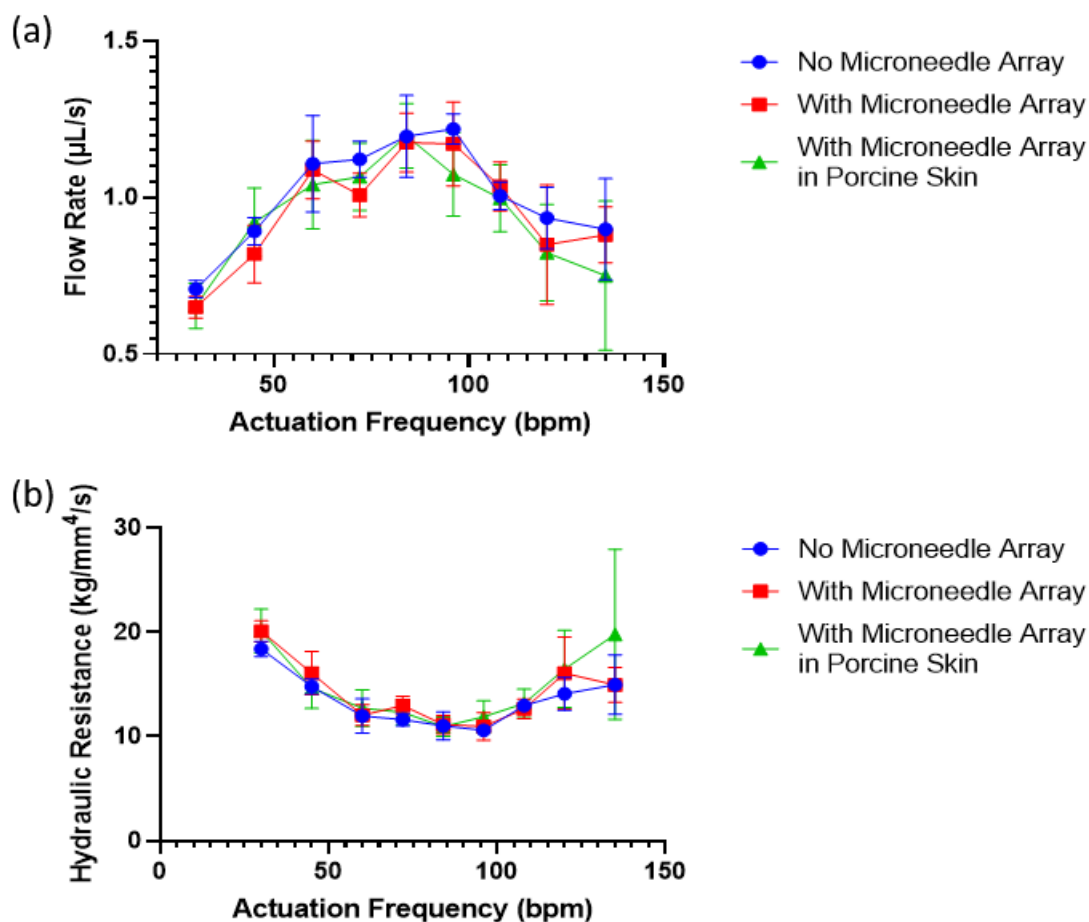


**Figure 3.9: Detailed characterization of (a) flow rate and (b) hydraulic resistance against actuation frequency with a microneedle array and a piece of porcine skin involved.** The model device (device #2, flow channel width 2300  $\mu\text{m}$ , depth 80  $\mu\text{m}$ ) was used, and the flow was characterized under nine different actuation frequencies between 30 and 135 bpm and a constant actuation pressure of 60 bpm. The difference in flow rate and hydraulic resistance between the three experimental groups was statistically insignificant ( $p > 0.1$ ) at all nine actuation frequencies.

### **3.3.4 Flow rate profile of devices with various flow channel widths across physiologically relevant actuation frequency and pressure spectra.**

Similar to the model device, the flow rate across four other devices (device 3, flow channel width 4600  $\mu\text{m}$ ; device 8, flow channel width 4025  $\mu\text{m}$ ; device 10, flow channel width 3450  $\mu\text{m}$ ; and device 12, flow channel width 2875  $\mu\text{m}$ ) was characterized over a wide range of physiologically relevant actuation frequencies and pressures. Twelve different actuation frequencies between 30 and 180 bpm were used to actuate the flow, and the results are shown in Figure 3.10, while the actuation pressure was held constant at 100 mmHg. We found that there was a negative correlation between the flow rate and the actuation frequency across the entire physiological actuation frequency range for devices 3, 8, and 10 ( $p < 0.01$ ). On the other hand, the correlation between the flow rate and the actuation frequency was positive for devices 2 and 12 ( $p < 0.001$ ), yet there was a pronounced drop in the flow rate at higher frequencies for both of these devices. The main difference between the two groups of devices is that devices 2 and 12 have narrower flow channels as compared to the other three devices tested (Table 3.1).

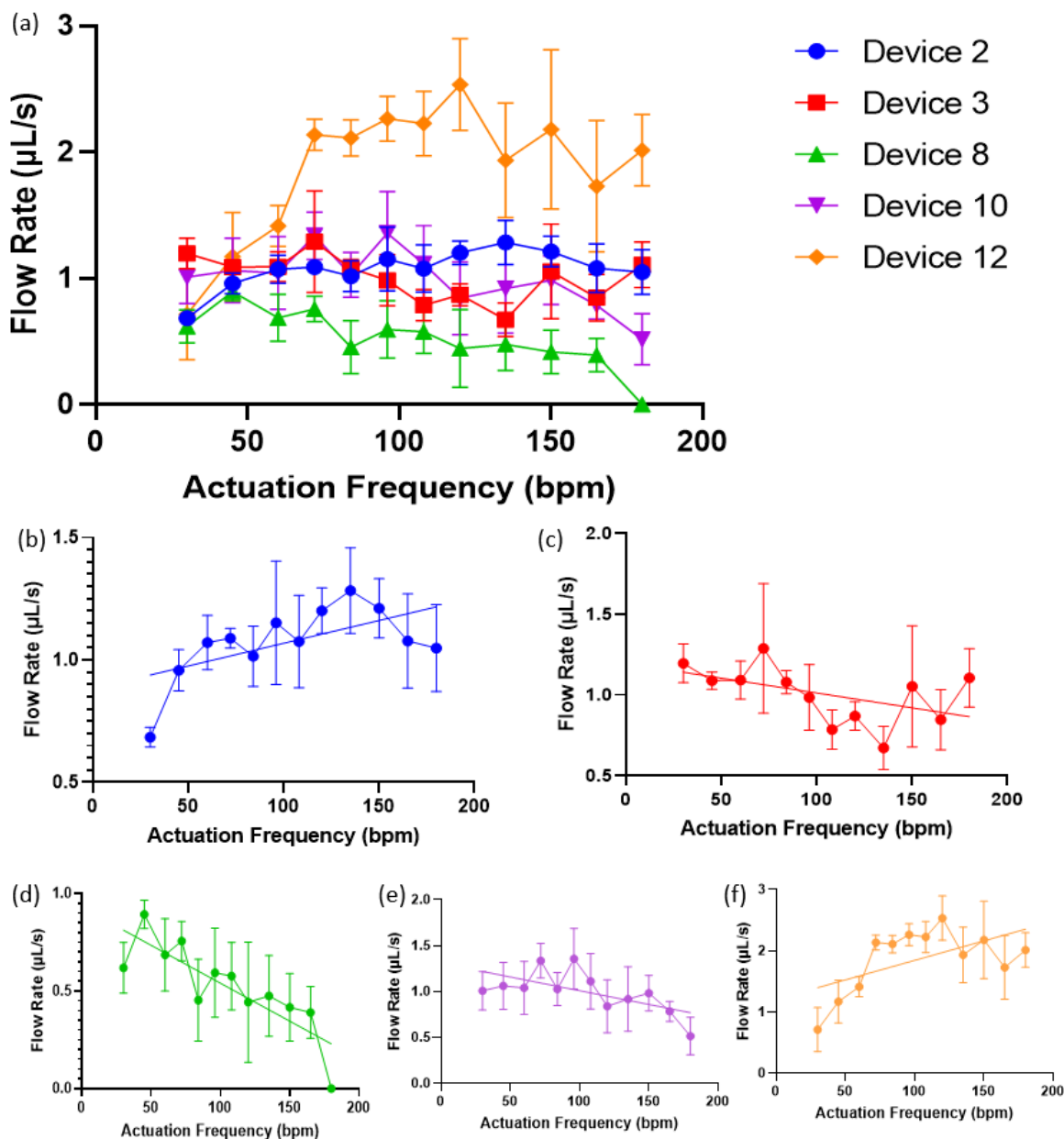


**Figure 3.10: Detailed characterization of flow rate against actuation frequency for devices at five flow channel widths.** (a) Plot of flow rate against actuation frequency for all five devices. (b) Plot of flow rate against actuation frequency for device #2 (trial 2 from Figure 3.8a, flow channel width 2300 μm) (Linear regression:  $y = 0.001858x + 0.8829$ ,  $r^2 = 0.1985$ ,  $p = 0.0003$ ). (c) Plot of flow rate against actuation frequency for device #3 (flow channel width 4600 μm) (Linear regression:  $y = -0.001838x + 1.196$ ,  $r^2 = 0.1146$ ,  $p = 0.0082$ ). (d) Plot of flow rate against actuation frequency for device #8 (flow channel width 4025 μm) (Linear regression:  $y = -0.003889x + 0.9292$ ,  $r^2 = 0.4458$ ,  $p < 0.0001$ ). (e) Plot of flow rate against actuation frequency for device #10 (flow channel width 3450 μm) (Linear regression:  $y = -0.002991x + 1.310$ ,  $r^2 = 0.1913$ ,  $p = 0.0005$ ). (f) Plot of flow rate against actuation frequency for device #12 (flow channel width 2875 μm) (Linear regression:  $y = 0.006373x +$

1.207,  $r^2 = 0.2427$ ,  $p < 0.0001$ ). Twelve actuation frequencies from 30 to 180 bpm were used for all four devices. The flow channel depth was 80  $\mu\text{m}$  for all devices, and the actuation pressure was held at 100 mmHg.

The flow rate of the same batch of microfluidic devices in the previous test was also characterized under a series of seven actuation pressures between 75 and 225 mmHg at a constant actuation frequency of 60 bpm. The results are shown in Figure 3.11. The flow rate was found to be positively correlated to the actuation pressure for all five devices ( $p < 0.01$ ) except for device 8 (flow channel width 4025  $\mu\text{m}$ ). For device 8, there was a vague, but not statistically significant, positive correlation between the actuation pressure and the flow rate ( $p = 0.1177$ ).

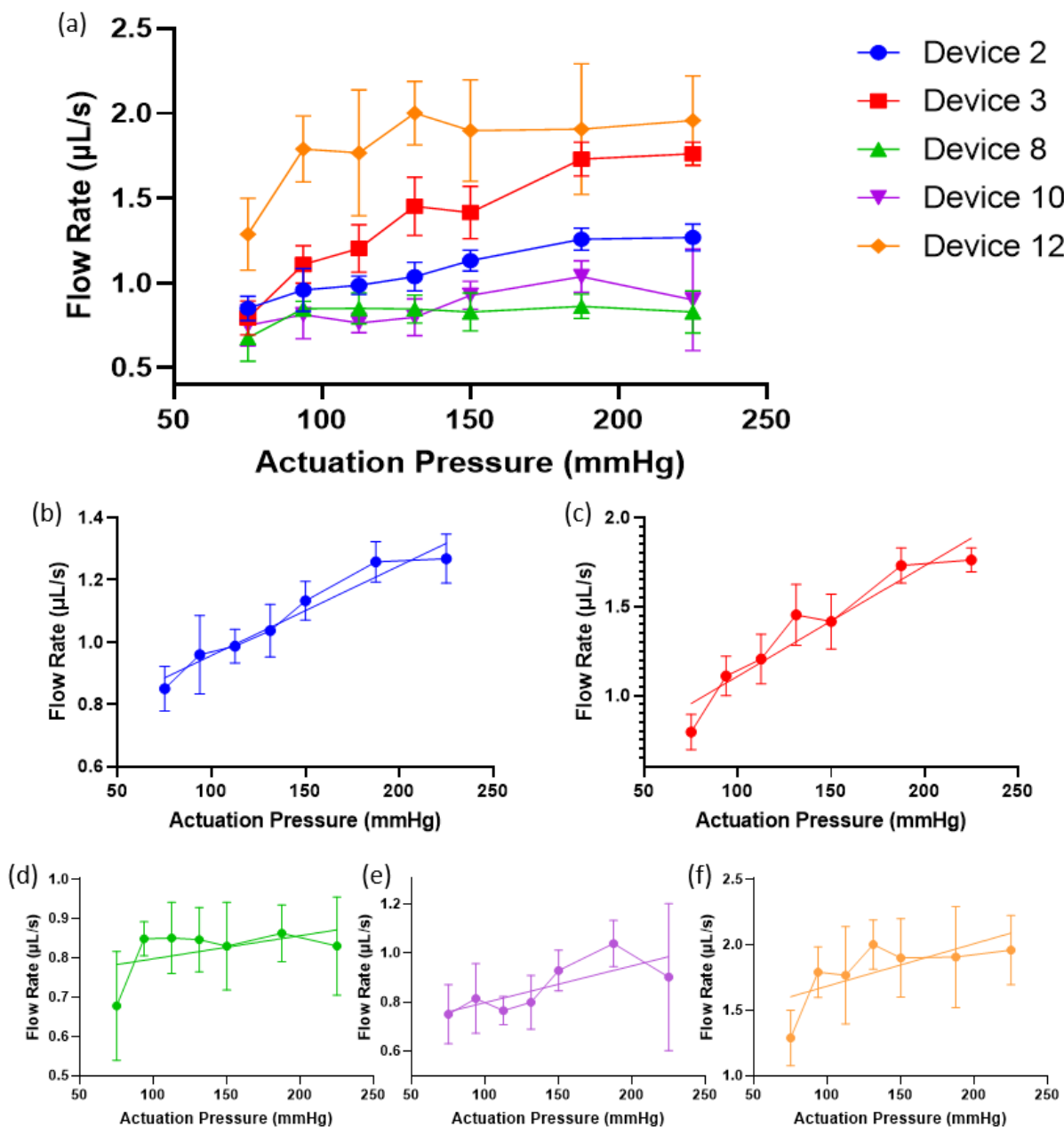


**Figure 3.11: Detailed characterization of flow rate against actuation pressure for devices at five flow channel widths.** (a) Plot of flow rate against actuation pressure for all five devices. (b) Plot of flow rate against actuation pressure for device #2 (the “60 bpm” curve from Figure 3.8b, flow channel width  $2300\ \mu\text{m}$ ) (Linear regression:  $y = 0.002884x + 0.6689$ ,  $r^2 = 0.7597$ ,  $p < 0.0001$ ). (c) Plot of flow rate against actuation pressure for device #3 (flow channel width  $4600\ \mu\text{m}$ ) (Linear regression:  $y = 0.006208x + 0.4881$ ,  $r^2 = 0.8030$ ,  $p < 0.0001$ ). (d) Plot of flow rate against actuation pressure for device #8 (flow channel width  $4025\ \mu\text{m}$ ) (Linear regression:  $y = 0.0005893x + 0.7388$ ,  $r^2 = 0.07253$ ,  $p = 0.1177$ ). (e) Plot of flow rate against actuation pressure for device #10 (flow channel width  $3450\ \mu\text{m}$ ) (Linear regression:  $y = 0.001497x + 0.6481$ ,  $r^2 = 0.1985$ ,  $p = 0.0073$ ). (f) Plot of flow rate against actuation pressure for device

#12 (flow channel width 2875  $\mu\text{m}$ ) (Linear regression:  $y = 0.003241x + 1.360$ ,  $r^2 = 0.2006$ ,  $p = 0.0070$ ). Seven actuation pressures from 75 to 225 mmHg were used for all four devices. The flow channel depth was 80  $\mu\text{m}$  for all devices, and the actuation frequency was held at 60 bpm.

The flow rate data as plotted in Figures 3.10 and 3.11 could be rearranged for the investigation of the effect of the flow channel width on the flow rate at each activation frequency and pressure. Figure 3.12 plots the flow rate against the channel width at five different actuation frequencies (30, 60, 96, 120, and 150 bpm). The actuation pressure was 100 mmHg for all flow results plotted in this figure. The flow rate was positively related to the flow channel width only at an actuation pressure of 30 bpm, and this correlation was statistically significant ( $y = 0.0001614x + 0.2876$ ,  $p = 0.0210$ ). The flow rate had no significant correlation with the flow channel width at 60 bpm ( $y = -0.0001195x + 1.473$ ,  $p = 0.0942$ ). At higher actuation frequencies (96, 120, and 150 bpm), there was a significant negative slope in the correlation between the flow rate and the channel width. This also confirms the finding that the flow rate in wider flow channels is more negatively affected by higher actuation frequencies than that in narrower flow channels.

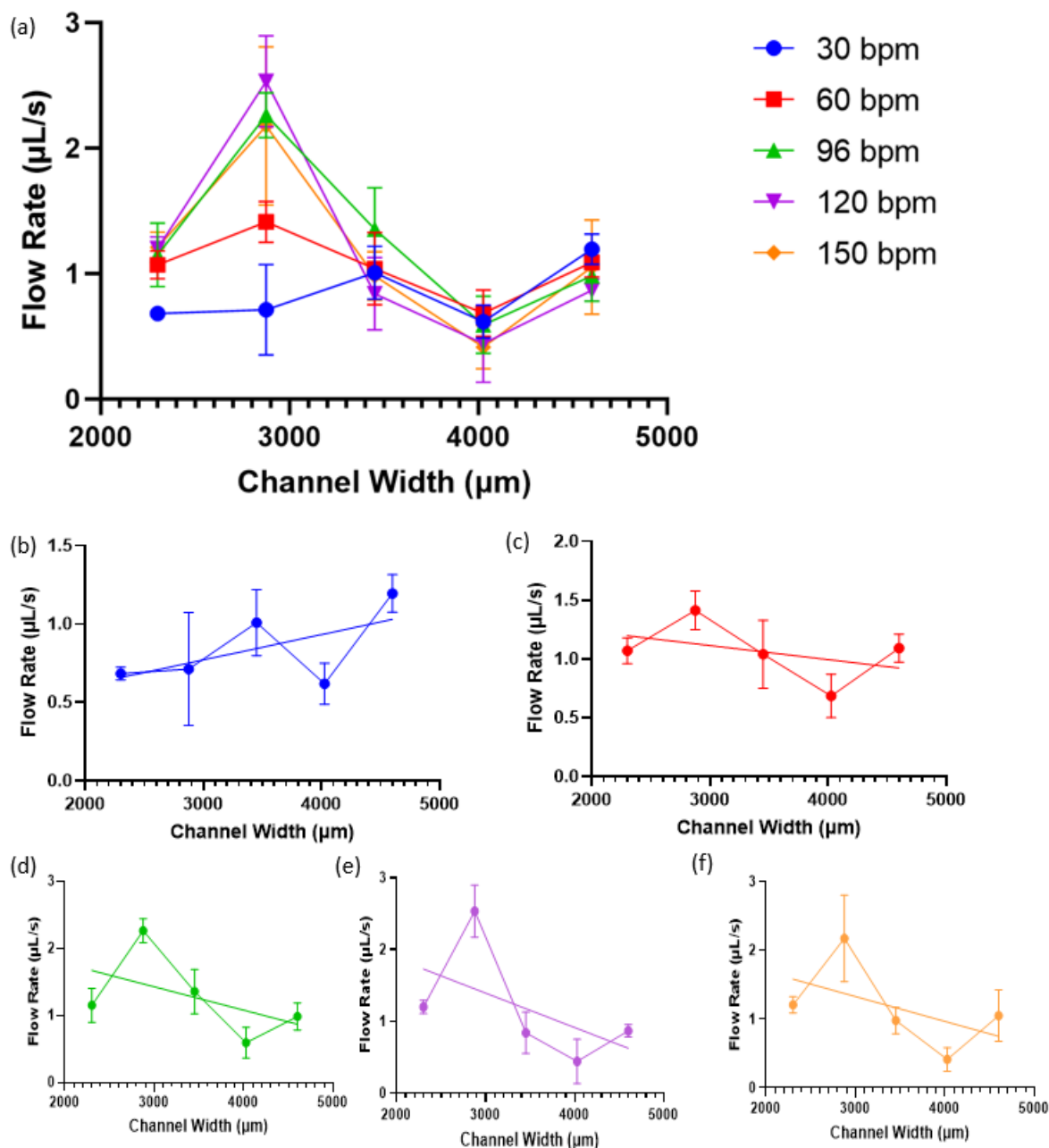


**Figure 3.12: Detailed characterization of flow rate against flow channel width at six different actuation frequencies.** (a) Plot of flow rate against flow channel width at five different actuation frequencies (30, 60, 90, 120, and 150 bpm). (b) Plot of flow rate against flow channel width at 30 bpm ( $y = 0.0001614x + 0.2876$ ,  $r^2 = 0.2106$ ,  $p = 0.0210$ ). (c) Plot of flow rate against flow channel width at 60 bpm ( $y = -0.0001195x + 1.473$ ,  $r^2 = 0.1170$ ,  $p = 0.0942$ ). (d) Plot of flow rate against flow channel width at 96 bpm ( $y = -0.0003483x + 2.472$ ,  $r^2 = 0.2249$ ,  $p = 0.0166$ ). (e) Plot of flow rate against flow channel width at 120 bpm ( $y = -0.0004787x + 2.829$ ,  $r^2 = 0.2661$ ,  $p = 0.0083$ ). (f) Plot of flow rate against flow channel width at 150 bpm ( $y = -0.0003615x + 2.417$ ,  $r^2 = 0.2026$ ,  $p = 0.0240$ ). The flow

channel depth was 80  $\mu\text{m}$  for all devices, and the actuation pressure was held constant at 100 mmHg.

Similarly, the flow characterization data for the five devices could be rearranged to generate a plot of flow rate against flow channel width at each activation pressure, as shown in Figure 3.13. The flow rate was plotted against the flow channel width at five different actuation pressures (75, 113, 150, 188, and 225 mmHg), while the actuation frequency was held constant at 60 bpm. Surprisingly, the correlation between the flow rate and the flow channel width was insignificant at any actuation pressure, which may suggest that the flow channel width does not play a role in the flow rate at 60 bpm, which confirms the finding in Figure 3.12b.

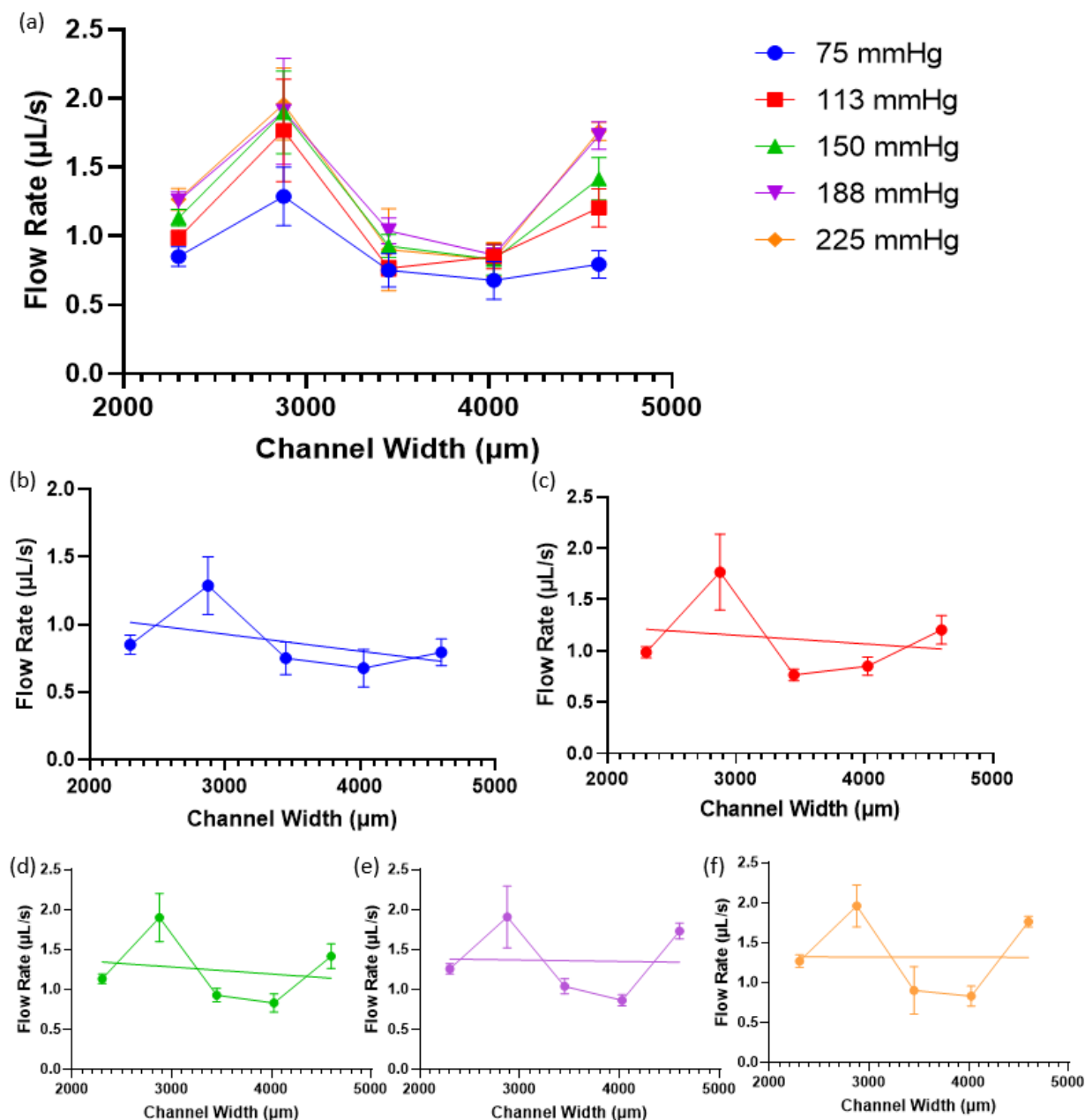


**Figure 3.13: Detailed characterization of flow rate against flow channel width at six different actuation pressures.** (a) Plot of flow rate against flow channel width at five different actuation pressures (75, 113, 150, 188, and 225 mmHg). (b) Plot of flow rate against flow channel width at 75 mmHg ( $y = -0.0001255x + 1.305$ ,  $r^2 = 0.1695$ ,  $p = 0.0409$ ). (c) Plot of flow rate against flow channel width at 113 mmHg ( $y = -8.372 \times 10^{-5}x + 1.404$ ,  $r^2 = 0.0269$ ,  $p = 0.4101$ ). (d) Plot of flow rate against flow channel width at 150 mmHg ( $y = -8.773 \times 10^{-5}x + 1.544$ ,  $r^2 = 0.02984$ ,  $p = 0.4090$ ). (e) Plot of flow rate against flow channel width at 188 mmHg ( $y = -1.720 \times 10^{-5}x + 1.419$ ,  $r^2 = 0.001041$ ,  $p = 0.8783$ ). (f) Plot of flow rate against flow channel width at 120 bpm ( $y = -2.302 \times 10^{-6}x + 1.327$ ,  $r^2 =$

0.0003512,  $p = 0.9852$ ). The flow channel depth was  $80\ \mu\text{m}$  for all devices, and the actuation frequency was held constant at 60 bpm.

### 3.4 Assembly of an Integrated Patch-Pump Prototype.

As mentioned previously, the end goal of this project is to fabricate a slim, powerless integrated, pulse-driven patch-pump used to deliver insulin painlessly through the skin. Two patch-pump prototypes have been developed by our team so far. The first prototype of the wearable microfluidic patch-pump, as shown in Figure 3.14a, was made by connecting the outlet (“+” end as shown in Figure 1.1c) of the flow channel of the microfluidic device with the inlet of a microneedle array using a short piece of Tygon tubing. Alternatively, the microfluidic device and the microneedle array could be housed with a 3D-printed casing and connected with a very short piece of Tygon tubing.

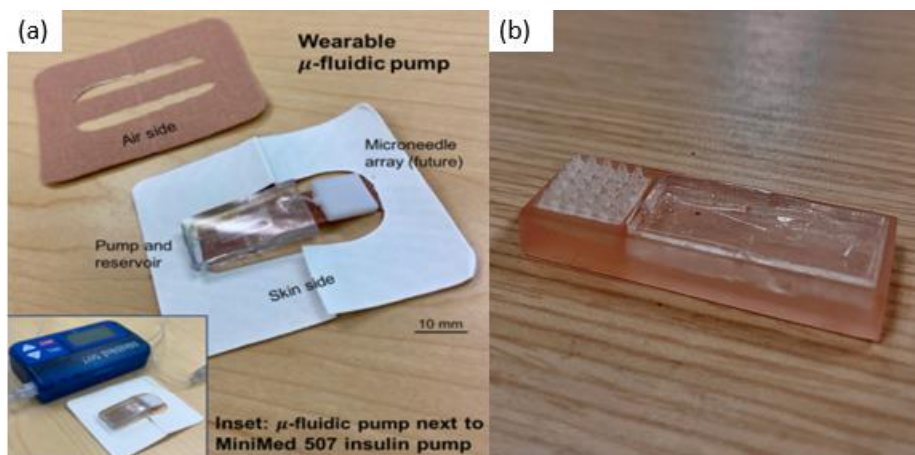


**Figure 3.14: Current Integrated Patch-Pump Prototypes.** (a) First wearable microfluidic pump designed and photo by Anne Staples. (b) Integrated microfluidic pump in casing designed using SOLIDWORKS by Ryan Zolovick, photo by Jenna Sims.

# Chapter 4

## Discussion

### 4.1 Fabrication of Microfluidic Devices and Microneedle Arrays

We have demonstrated the successful fabrication of microfluidic devices with a method of photolithography followed by replica molding and plasma bonding. This was indicated by the fact that most devices showed triangular flow channels and rectangular actuation channels with very high fidelity. Furthermore, most devices had an intact membrane and could be used to drive fluid flow in the presence of alternating pressurized air-vacuum cycles. In contrast, the 3D printing method, although much more time-efficient and less difficult, was unable to show the fine channel structures inside the devices due to the resolution constraints (Figure 4.1). In fact, the resolution of the resin used (Elastic 50A) had a relatively low resolution 100  $\mu\text{m}$ , which is far from sufficient to accurately print the fine channel features inside the device. Also, no soft resin provided by Formlabs could achieve a resolution below 50  $\mu\text{m}$ .<sup>59,60</sup>

Therefore, we will continue to fabricate devices using the soft lithography technique, which has also been proven effective by previous experiments.<sup>61-67</sup> In the aspect of master mold fabrication, however, a potential alternative is to fabricate master molds using stereolithographic 3D printing in lieu of photolithography. This method has been proven effective by multiple studies in Brendon Baker's research group at the University of Michigan.<sup>68-71</sup> A potential shortcoming of this method is the low resolution as mentioned before, but we expect it this method to work more successfully as compared to the 3D printed microfluidic devices. Since all channel structures are designed on the external surface of the master mold, it can be printed more accurately as compared to the microfluidic devices, in which all the fine structures are on the interior and therefore subject to fouling. More importantly, significantly lower resolution is required to print the channel designs on the master mold than it is for the fine membrane inside the microfluidic devices. In addition, hard resins can be used to make master molds—some hard Formlabs resins have a resolution as fine as 25  $\mu\text{m}$ , as compared to 50 or 100  $\mu\text{m}$  for soft resins.<sup>72,73</sup> This method is especially favorable over traditional photolithography in fabricating master molds for devices with deeper channels because the resolution requirement is not as high and because SU-8 2075 severely retracts towards the center at a high layer thickness (Figure 4.1a).

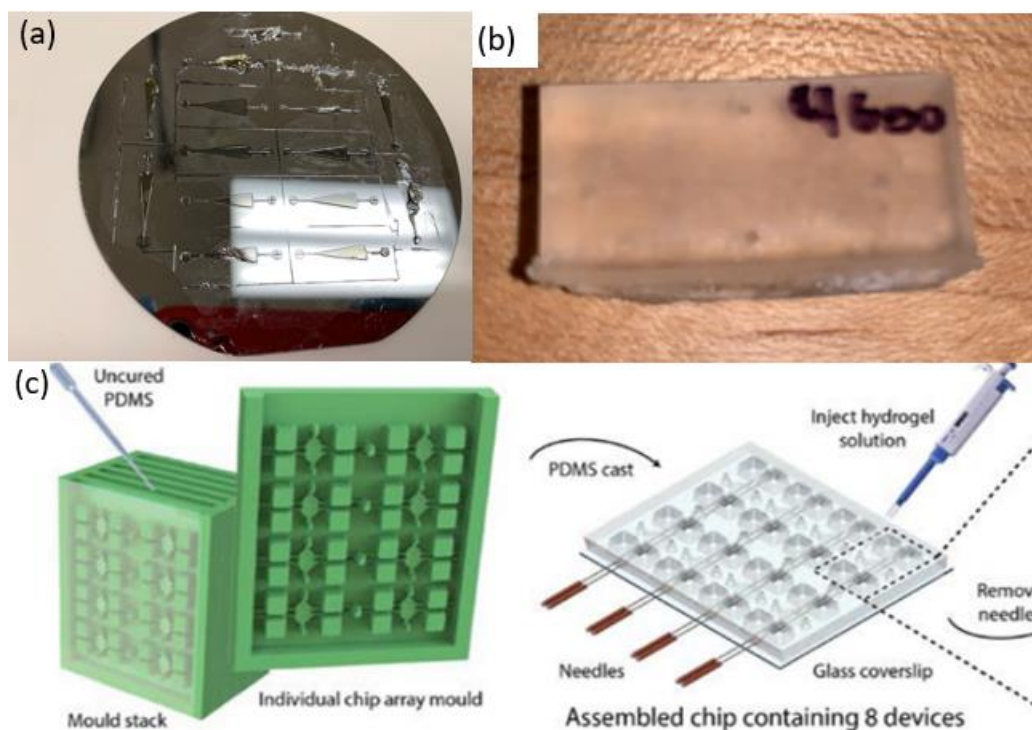


**Figure 4.1: Limitation in current microfluidic device fabrication methods and alternative solution.** (a) Master mold of flow channel for device S2 with flow channel widths shown in Table 3.1 and depth of 200  $\mu\text{m}$ . There are visible imperfections due to significant retraction of the SU-8 photoresist towards the center upon soft baking. (b) 3D printed microfluidic device with Formlabs Elastic 50A resin. No fine structures are shown in the device. (c) Schematic of 3D printed master mold and PDMS microfluidic layer replica casted from the printed master molds.<sup>68</sup> Reproduced/Adapted from ref. 68 with permission from The Royal Society of Chemistry.

3D printing was able to fabricate hollow microneedle arrays with high fidelity since the resolution requirement is much lower than that of the microfluidic devices. We demonstrated that almost most prototypes were able to deliver fluid into the skin, suggesting that the hollowness and sharpness of the microneedle arrays were desirable (Figure 3.6 and Table 3.3). The microneedle arrays will be further discussed in the next section (4.2).

## 4.2 Penetration testing of microneedle arrays and comparison of microneedle array prototypes.

As shown in Figure 3.4, six microneedle array prototypes were designed using COMSOL Multiphysics. From the penetration testing as shown in Figure 3.6 and Table 3.3, all nine microneedle arrays were able to penetrate the porcine skin as shown by the creation of pores. Almost all microneedle arrays were able to deliver dyed water into the porcine dermis, since the

epidermal thickness was only less than 0.2 mm.<sup>74</sup> This is demonstrated by the retention of the dye within the skin after the dye on the skin surface was blotted as described in section 2.4. Microneedle array #7 did not show penetration of dye into the skin, which could be due to the relatively dull microneedle tips which were not sharp enough to completely embed in the skin. The mean penetration depth (1.433 mm) was the highest for microneedle array prototype #8, which follows the revised  $5 \times 5$  design with relatively sharp microneedles. This microneedle array also showed a relatively low standard deviation (0.153 mm) across the three locations, suggesting that the microneedle array was uniformly arranged so that it could penetrate the skin equally well at multiple different locations. As opposed to designs such as prototype #3 which only delivered fluid at one location, the selected prototype was much more efficient in fluid delivery.

In addition, the selected microneedle array model was made of Surgical Guide Resin, which is biocompatible and designed for medical use.<sup>75</sup> Therefore, to minimize side reactions, this microneedle array prototype is also very desirable.

### 4.3 Flow testing across microfluidic devices.

Before testing the microfluidic devices on the human body for insulin delivery, we should be able to fully characterize the devices *ex vivo* to understand how the flow characteristics change with the actuation frequency and pressure. This characterization process is necessary to enhance successful insulin delivery to diabetic patients for two reasons. First, in order for the device to achieve successful glycemic control in diabetic patients, it must be able to respond to heart rate and blood pressure of the human subject in a specific way. Specifically, the flow rate should be inversely correlated to the heart rate, especially for heart rates higher than the resting heart rate range. This is because elevated heart rate typically occurs during exercise, and more vigorous exercise would lead to less demand for insulin in diabetic patients due to a drop in blood glucose.<sup>76</sup> Second, the variation in how their delivery rate responds to the heart rate and blood pressure (which are simulated by the actuation frequency and pressure, respectively) is important for addressing individual patients' specific insulin demands.

In the five microfluidic devices with detailed flow rate profiles so far (as shown in Figures 3.10), our results indicate that the flow rate across devices 2 and 12 exhibits a significantly positive correlation ( $p < 0.05$ ) with the actuation frequency according to the linear regression shown in Figure 3.10b and 3.10f. However, both devices experienced a drop in the flow rate at higher actuation frequencies (Figure 3.10b and 3.10f). This finding confirmed some previous characterization with device 2, as shown in Figure 3.8a and 3.9a. For the other three devices, the flow rate showed a significant decreasing trend with an increase in actuation frequency ( $p < 0.05$ , Figure 3.10c-e). The primary difference between these devices was the flow channel width, since devices 2 and 12 had narrower flow channels as compared to the other devices. This leads to the preliminary conclusion that wider flow channels were more desirable for insulin delivery as compared to narrower channels.

It is counterintuitive that the flow rate across devices 3, 8, and 10 drops with increasing actuation frequency at physiological actuation frequencies and pressures because contractions were more frequent at actuation frequencies. However, it is quite clear that this trend is due to the lack of time for the elastomeric membrane to completely collapse and re-expand at higher frequencies, which results in significantly less flow driven by each membrane contraction. To demonstrate this, images were taken to compare the mechanisms of flow at a low frequency (30 bpm) and a high frequency (180 bpm) (Figure 4.2). From this image, we can see that the flow channel almost completely collapsed at 30 bpm, driving all fluid to the center (Figure 4.2a). In contrast, the flow channel only slightly collapsed at 180 bpm, with very small amounts of fluid movement occurring in each contraction.

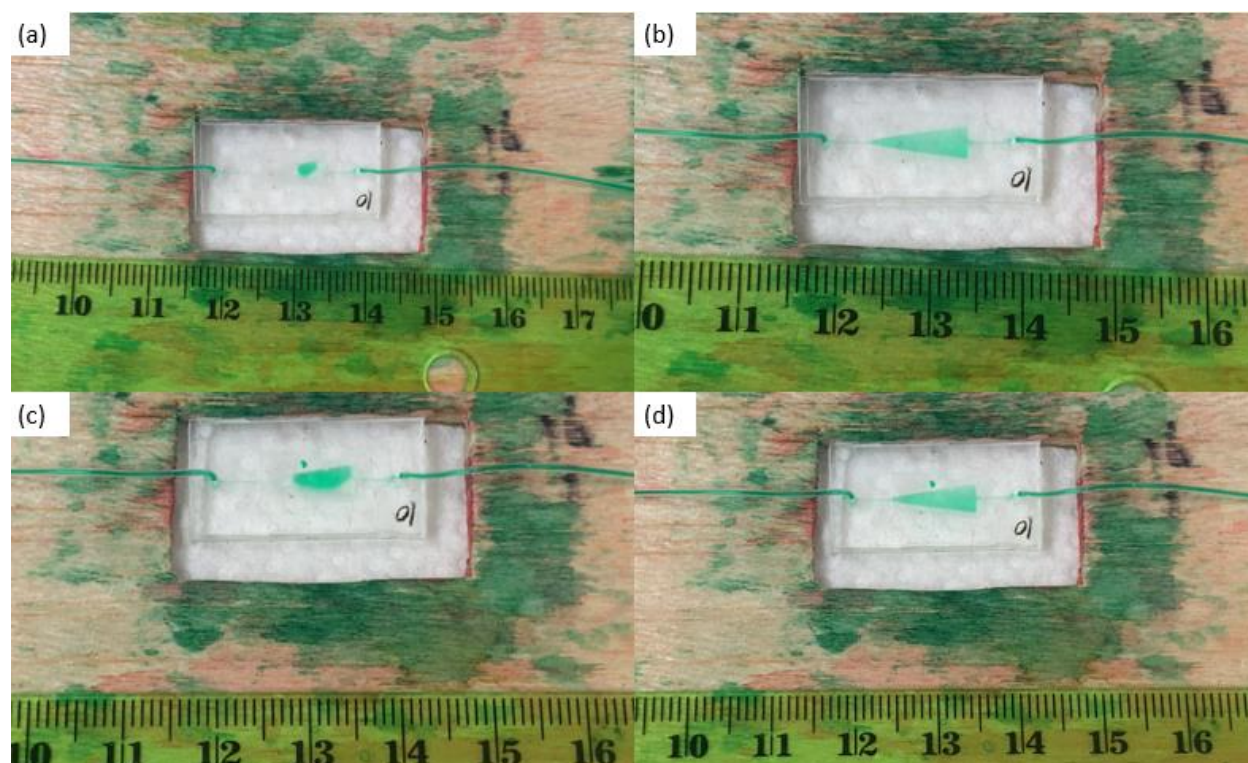


**Figure 4.2: Collapse and re-expansion of flow channel at 30 and 180 bpm.** (a) Device 10 (flow channel width 3450  $\mu\text{m}$ , depth 80  $\mu\text{m}$ ) during the collapse (“systole”) phase when actuated at 30 bpm. (b) Device 10 during the re-expansion (“diastole”) phase when actuated at 30 bpm. (c) Device 10 during the collapse (“systole”) phase when actuated at 180 bpm. (d) Device 10 during the re-expansion (“diastole”) phase when actuated at 180 bpm. The flow was actuated at 100 mmHg in both scenarios.

This phenomenon occurred for all five devices, but its effect was more pronounced in devices with wider flow channels. Therefore, the net effect of higher actuation frequencies on the flow was more negative for devices with wider flow channels than it was for devices with narrower flow channels. We postulate that it takes more time for wider flow channels to collapse and re-expand as compared to the narrow channels due to a higher net membrane deflection, according to Equation 4.1.<sup>77</sup>

$$\delta_{max} = \frac{w_m}{4} \left( \frac{3\Delta P w_m}{\bar{E} t_m} \right)^{\frac{1}{3}} \quad (4.1)$$

Where,  $\delta_{max}$  is the maximum deflection of the elastic membrane,  $w_m$  is the width of the elastic membrane (which is equal to the width of the flow channel in this case),  $t_m$  is the thickness of the elastic membrane,  $\Delta P$  is the applied pressure, and  $\bar{E} = \frac{E}{(1-\nu)^2}$ , where E is the Young's modulus and  $\nu$  is the Poisson ratio of the material. All properties are listed in Table 4.1 below.

**Table 4.1: Estimated maximum membrane deflection for the five device designs we have used.** The Young's modulus (for the PDMS membrane made of 5:1 PDMS:curing agent mixture) is based on the article by Park et al. (2010),<sup>78</sup> and the Poisson's ratio is from the assumption that the material is incompressible.

Material and Actuation Parameters	Flow Channel Width $w_m$ ( $\mu\text{m}$ )	Maximum Membrane Deflection $\delta_{max}$ ( $\mu\text{m}$ )
	2300	334
$E = 1000$ kPa	2875	450
$t_m = 20$ $\mu\text{m}$	3450	574
$\nu = 0.5$	4025	705
$\Delta P = 100$ mmHg	4600	842

In the aspect of the actuation pressure, all five devices except for device 8 (flow channel width 4025  $\mu\text{m}$ ,  $p = 0.1177$ ) showed a significantly positive correlation between the flow rate and the actuation pressure. This result is completely expected because a higher deformation of the elastic membrane would result from a higher actuation pressure from Equation 4.1.<sup>77</sup>

The positive relationship is desirable for insulin delivery because hypertensive diabetic patients are in greater demand of insulin as compared to non-hypertensive patients due to the increased insulin resistance in hypertensive patients.<sup>79</sup> However, device 8, the only device that did not have a significant correlation between the flow rate and the actuation pressure, is more favorable for non-hypertensive patients because the insulin delivered to the body because elevated blood pressure could be due to stress rather than chronic hypertension.<sup>80-82</sup> The reason why this device did not exhibit the characteristic relationship is currently unknown, and further investigation using more replicates of similar devices and computational modeling (as described in section 5.3) is needed to help us understand the physics behind this finding.

However, the maximum deflection of the membrane is calculated to be between 334 and 842  $\mu\text{m}$  for a typical device with a flow channel width 3450  $\mu\text{m}$  at an actuation pressure of 100 mmHg. This suggests that the flow is probably not limited by the deflection of the membrane, but rather by the depth of the flow channel (80  $\mu\text{m}$  for most of this study and previous work in our

laboratory), which is much less than the maximum deflection, in the case of lower actuation frequencies, and the time taken to collapse and re-expand the flow channel, in the case of higher actuation frequencies. Therefore, if the membrane deflection was not limited by the channel depth, the inverse relationship between the actuation frequency and flow rate would be more pronounced. This would make the device more ideal for insulin delivery.

Upon the addition of the 3D-printed hollow microneedle array and the porcine skin, no alteration of the flow rate or the hydraulic resistance was observed. Although previous findings suggest that hollow microneedle arrays are inherently associated with a hydraulic resistance, our study suggests that neither the microneedle array nor the porcine skin had a significant contribution to the total hydraulic resistance of the system.<sup>83,84</sup> This might be because the hydraulic resistance contributed by the microneedle array and the porcine skin is negligible as compared to that contributed by the microfluidic pump, which employs a sensible amount of pressure to generate a small flow rate around 1  $\mu\text{L/s}$ . This finding suggests that the microneedle arrays or porcine skin samples may not be necessary for future flow rate testing experiments, even though adding these components will make the testing more accurately recapitulate testing on the human wrist.

## 4.4 Limitations of study

### 4.4.1 Fabrication of master molds and microfluidic devices.

The soft lithography protocol we used in fabricating the microfluidic devices is still imperfect and needs to be improved. Many procedures in our protocol could lead to variability in performance across different devices, including bubbling or uneven thickness of the photoresist layer on the master mold, slight variations in the mixing ratio of the PDMS base and the curing agent, and most importantly, variations in the manual alignment process during plasma bonding. The last point is very important because this can significantly alter the specific locus in the device where the membrane is maximally deformed, while we do not know the exact correlation between the locus of maximum collapse and the flow rate of the fluid, which is worth investigating.

In the aspect of master mold fabrication, although previous protocols indicate that SU-8 can be used to fabricate thicker photoresist layers,<sup>85-87</sup> a significant limitation is that SU-8 experiences retraction towards the center and therefore severe layer thickening at a relatively high photoresist layer thickness (200  $\mu\text{m}$ ), as shown in Figure 4.1a. Therefore, to fabricate thicker channel designs, a promising alternative is 3D printing master molds followed by replica molding, as discussed in section 4.1.<sup>68-71</sup>

### 4.4.2 Fabrication and penetration testing of microneedle arrays.

An obvious limitation observed during the penetration testing of microneedle arrays is the small amount of overflow on the superficial skin surface, which would be problematic if these

microneedle arrays were used for insulin injection on the human skin. We believe that this is due to the fact that the microneedle arrays were not completely and firmly embedded in the skin. This can be solved by redesigning the microneedle structure so that the microneedles would be firmly embedded in the skin to result in more effective penetration without significant overflow or leakage.

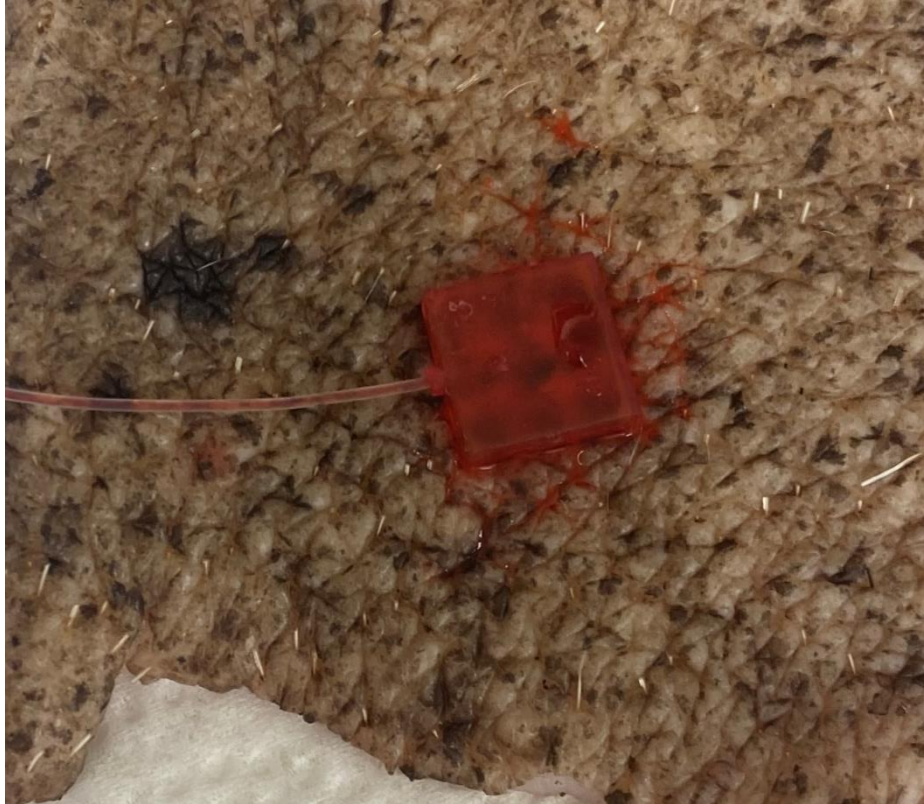


**Figure 4.3: Delivery of red-dyed water to porcine skin through a microneedle array.** There is slight, but visible, spill of the dye at the surface of the skin. (Photo: Jenna Sims)

Another limitation is that our microneedle arrays do not control insulin delivery based on the blood glucose level. In fact, more sophisticated closed-loop microneedle arrays have been developed by previous researchers.<sup>32,88-91</sup> In these studies, hydrogel-based solid microneedle arrays were typically fabricated. These microneedle arrays were used to encapsulate insulin-containing vesicles activated using a glucose-sensing enzyme, commonly glucose oxidase (GOx). However, due to these sophisticated designs, these microneedle arrays are more difficult to make and more expensive as compared to our design.

### 4.4.3 Flow testing.

In the aspect of flow rate testing, most devices still show significant variability across trials even with identical experimental conditions as shown by the error bars in Figures 3.7-3.13, which represent standard deviations. The standard deviation was often over 10% (and occasionally over 20%) of the average flow rate, which makes the results less promising than expected. This could be caused by a range of factors, including the positioning of the devices, differential membrane deformation at each actuation, as well as possible systematic and random errors in the flow rate measurement.

The flow rate measurement that we are currently using is still very time-consuming and error-prone. Accidental tilting of the camera while taking the video, inaccuracies in timing and reading while taking the data points, and delayed responses by the computer while replaying the video could all lead to random errors. These errors could significantly decrease the reliability of the results from the flow testing. Furthermore, this measurement method does not account for the reversal of flow direction and significant change of flow rate with respect to time, and cannot accurately capture flow that is too fast. According to qualitative preliminary testing, devices with deeper flow channels (depth 200  $\mu\text{m}$ ) could exhibit all three characteristics, which prevented us from collecting qualitative data from these devices using our current measurement technique. Therefore, we would like to transfer to a flow measurement technique that could capture the instantaneous flow rate, such as a microfluidic flow sensor.<sup>92,93</sup>

Furthermore, although we understand that the flow is driven by shear force created by the collapsing action of the elastomeric membrane against the flow channel, we do not understand the exact physics of the flow other than the points discussed in section 4.4.3. Therefore, testing of more replicates and computational modeling are necessary for us to explain the flow behavior at different channel design and actuation parameters.

Although *ex vivo* flow testing is a rapid and completely non-invasive method to characterize the flow performance of the devices as a function of channel design and actuation parameters, it does not very accurately recapitulate the performance two-layer versions of the devices on the human wrist. One of the reasons is that the devices may not fully re-expand on the wrist after the flow channel collapse by the pulse due to the absence of a vacuum source, making it more difficult to generate the flow. Another possible reason why the current testing protocol is not an accurate recapitulation is that the human heart and arteries do not spend an equal amount of time in systole and diastole.<sup>94-98</sup> In fact, the systolic time is almost always shorter than the diastolic time in each cardiac cycle, which has not been considered in our *ex vivo* testing model. To solve this, we can potentially improve the setup by setting unequal delay times in the Arduino program.

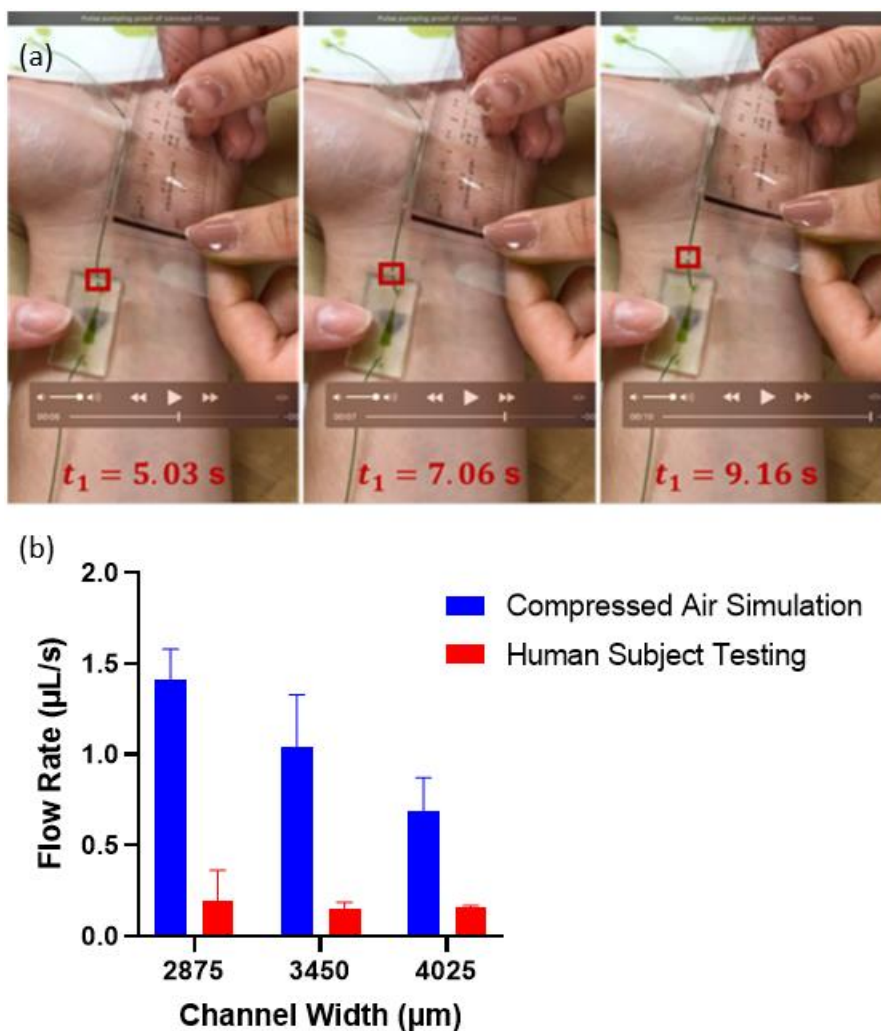


**Figure 4.4: Schematic of human subject testing and comparison of flow rates across devices at different flow channel widths actuated by compressed air and by radial arterial pulse on the human subject.** (a) Photos of human subject testing by Demitria Poulos, Tyler Rodriguez, Afreen Khoja, and Anne Staples. Flow of the fluid can be tracked by the position of the air bubble in the flow inlet at different time points. (b) Comparison between flow actuated by pressurized air and pulse-driven flow in human subjects across devices at flow channel widths of 2875, 3450, and 4025  $\mu\text{m}$ . For the data plotted in blue, the flow was characterized in this study at an actuation frequency of 60 bpm and an actuation pressure of 100 mmHg. Human subject testing with pulse-driven flow was performed by Jenna Sims, Tyler Kwak, Isabelle Mehochko, and Ryan Zolovick, at a pulse rate of 62 bpm, and results were plotted in red.

# Chapter 5

## Conclusions and Future Directions

### 5.1 Conclusions

In conclusion, we have fabricated a series of working insect-mimetic microfluidic devices targeted for insulin delivery using soft lithography techniques, and characterized the performance of the devices by testing the flow rate across each device actuated by pressurized air at different physiologically relevant experimental conditions. Through extensive testing, we have found that the flow rate across the devices generally showed a positive correlation with the actuation pressure. The flow rate showed a negative correlation with the actuation frequency for devices with wider flow channels ( $\geq 3450 \mu\text{m}$ ). For devices with narrower flow channels, however, the flow rate exhibited a positive relationship with the actuation frequency at lower actuation frequencies and a negative relationship at higher actuation frequencies. Ideally, we would like the flow rate to decrease with actuation frequency because diabetic patients generally do not need as much insulin at elevated heart rates. Also, we have designed and 3D-printed a series of microneedle array prototypes using COMSOL Multiphysics and Formlabs printers, respectively. Using penetration testing against a porcine skin sample, we determined a favorable prototype for transdermal insulin delivery, which is a  $5 \times 5$  prototype with sharp-tipped, syringe-shaped microneedles. The microneedle array was designed in such a way that it was completely compatible with the microfluidic device. Finally, we have assembled the microneedle arrays and microfluidic pumps into wearable microfluidic patch-pump prototypes.

### 5.2 Future Directions

#### 5.2.1 Further flow characterization of three-layer devices with compressed air and two-layer devices with human subjects.

To more fully and accurately characterize the performance of the microfluidic pumps with various flow channel widths and depths, we will fabricate more devices in the future to verify the relationship between the flow performance of the device and other parameters (actuation frequency, actuation pressure, and channel dimensions). To build devices that are specifically tailored to insulin delivery, we will further change dimensions of the devices so that the flow rate generated match the basal insulin delivery rate at resting heart rate and have a sharper decrease at elevated heart rates. In addition, as mentioned in section 4.4, the cardiac cycle is typically not 1/2-systole, 1/2-diastole, and some mathematical models use 1/3-systole and 2/3-diastole instead, so we can decrease the duration of the contraction phase and increase the duration of the re-expansion phase to more accurately recapitulate the native cardiac cycle.<sup>94-98</sup> Shapes of the flow

and actuation channels can also be changed to optimize the flow behavior to achieve ideal flow rates and flow patterns as discussed in section 4.3. Chatterjee et al. (2021) have generated a series of 11 channel designs, each showing different flow behavior, as shown in Figure 5.1.<sup>33</sup>

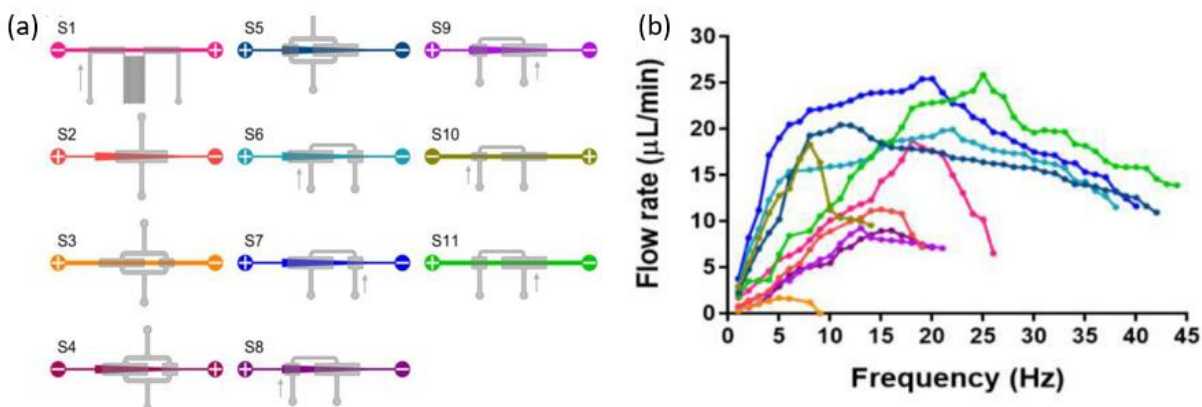


**Figure 5.1: Eleven insect-mimetic microfluidic channel designs by Chatterjee et al. (2021) and their performances at different actuation frequencies from 0 to 45 Hz.**<sup>33</sup> (a) Schematics of 3-layer single-channel devices designed by Chatterjee et al. (2021). For all channel designs, the flow channel is shown in color, with “-” indicating the expected flow outlet and “+” indicating the flow inlet. The actuation channel is shown in gray. (b) Plot of flow rate through the 11 devices against actuation frequency from 0 to 45 Hz. Republished with permission of IOP Publishing Ltd., from “Frequency-specific, valveless flow control in insect-mimetic microfluidic devices” by K. Chatterjee, P. M. Graybill, J. Socha, R. V. Davalos, and A. Staples, *Bioinspiration & Biomimetics*, Vol. 16, No. 3, © 2021 IOP Publishing Ltd; permission conveyed through Copyright Clearance Center, Inc.

Human testing of two-layer microfluidic devices has started in our laboratory recently and have been conducted by the senior design team (preliminary data are shown in Figure 4.4b), and we aim to recruit a wider range of human subjects in our study so that we can relate the flow performance with actual human pulse. Testing the devices using pressurized air is a very rapid method to characterize the devices, but it is far from accurate.

### 5.2.2 Optimization of device design with a genetic algorithm-guided approach.

Using data from human subject testing as well as pressurized air flow testing, we can optimize the device design using a genetic algorithm-guided approach to determine the optimal channel design to achieve a specific flow rate under a specific actuation frequency and pressure. The approach consists of three interconnected MATLAB programs, including the genetic algorithm, the model script, and the main function. This genetic algorithm-based approach can be used to design patch-pumps for individual needs based on their blood pressure, heart rate, and the target

flow rate. After optimization using this approach, a table of designs for each target flow rate can be generated similar to Figure 5.2c.

### 5.2.2.1 Genetic algorithm script.

The genetic algorithm script was modified from a script written by Ryan Senger of the Department of Biological Systems Engineering at Virginia Tech. This genetic algorithm was first used by Senger and Nazem-Bokaei in 2013 to determine cell composition of a strain of *Escherichia coli* and *Clostridium acetobutylicum*, but it can be applied to any complex optimization problem.<sup>99</sup> Briefly, the modified genetic algorithm starts with a user input of the initial guess of the chromosome (containing initial values for flow channel width, flow channel depth, flow channel length, and elastomeric membrane thickness), the heart rate and the blood pressure of the user, and the target flow rate. The genetic algorithm first randomly generates the initial generation (Generation 0) of chromosomes and calls the model script to calculate the objective function. Chromosomes will be sorted by increasing values of the objective function. The 25% best-performing chromosomes will be passed into the next generation, and the rest 75% will be discarded. Three different operators (BLX- $\alpha$  crossover, non-uniform mutation, and random generation) will be used to “mutate” the top 25% best-performing chromosomes to generate the rest 75% of the chromosomes in the next generation. The genetic algorithm then calls the model script to calculate the objective function for the new generation, and this process repeats until the pre-defined number of generations is reached. In the last generation, the best-performing chromosome with the channel design parameters and the theoretical flow rate will be outputted to the Command Window.

### 5.2.2.2 Model script.

The model script is a short, self-built script that calculates the objective function that will be minimized using the genetic algorithm as described in the previous section. The model script is called by the genetic algorithm to receive the chromosomes of channel design parameters. The model script then calls the main function to calculate the flow rate based on the channel design parameters. Upon receiving the calculated flow rate, the model script calculates the objective function, which is the difference between the calculated flow rate and the target flow rate normalized by the target flow rate:

$$e_i = |q_i - q_{target}/q_{target}| \times 100\% \quad (5.1)$$

Where,  $q_i$  is the flow rate for chromosome  $i$  calculated through the main function,  $q_{target}$  is the target flow rate, and  $e_i$  is the objective function to be minimized.

### 5.2.2.3 Main Function

The main function is a self-built MATLAB function that calculates the estimated flow rates using regressions fitted on experimental flow data. This function requires extensive inputs of experimental data, including channel design parameters (flow channel width, flow channel depth, flow channel length, and membrane thickness), user (or pressurized air actuation) parameters

(heart rate/actuation frequency, blood/actuation pressure), and resulting flow rates obtained in flow testing experiments. Correlations between the flow rate and other variables can be derived using these regressions. This program is still in progress due to insufficient generation of experimental data and the need to derive a more accurate regression model beyond linear and polynomial regressions.

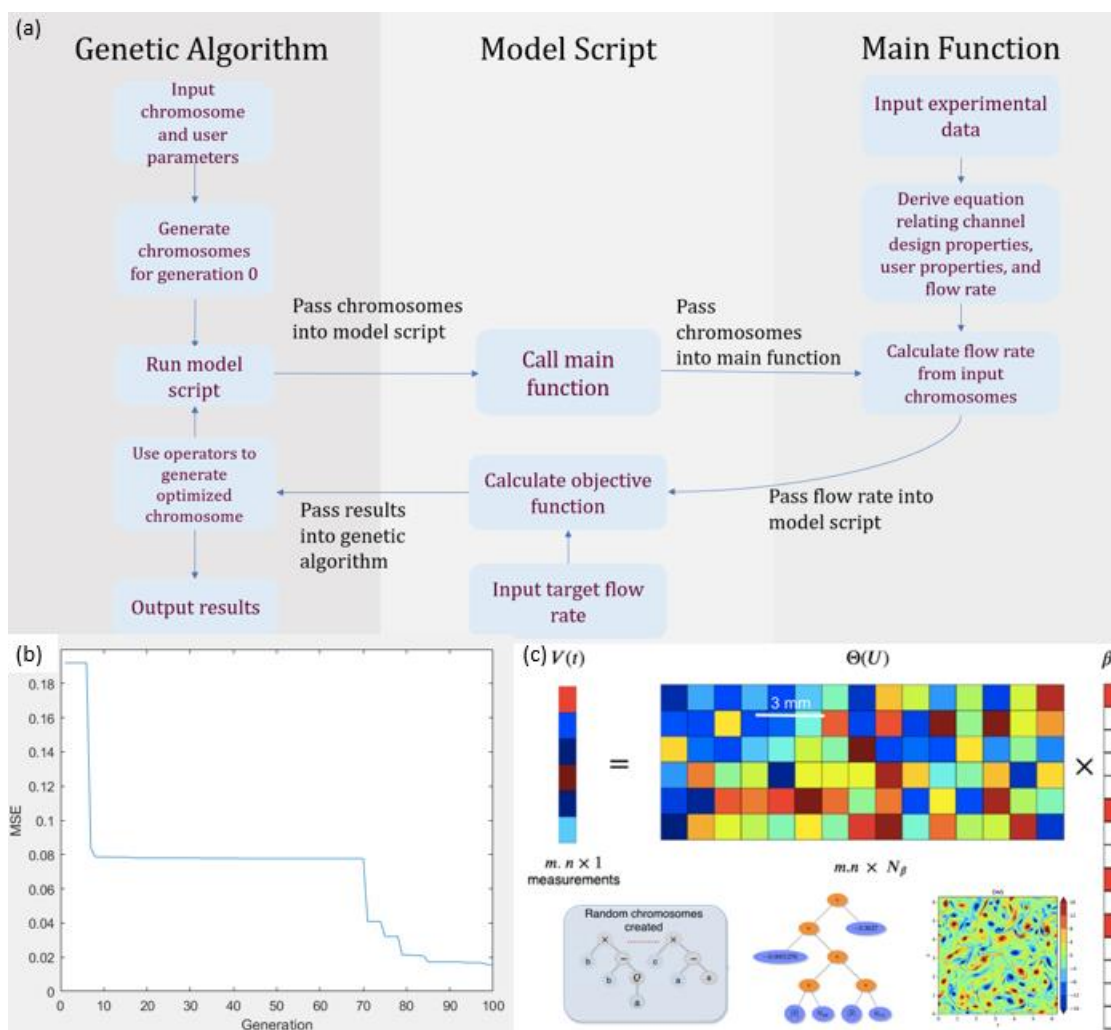


**Figure 5.2: A genetic algorithm-guided approach to optimize the channel design.** (a) Flowchart of a three-part genetic algorithm-guided approach built in MATLAB. (b) Previous work by Shuyu Zhang (2021, unpublished) to optimize the composition of a hydrogel by minimizing the mean squared error (MSE) between the calculated and target material properties using a three-part genetic algorithm. (c) An example table of designs that can be generated using a genetic algorithm-guided approach. Schematic is modified by Anne Staples from Vaddireddy et al. (2020).<sup>100</sup> Republished with permission of IOP Publishing Ltd., from “Feature engineering and symbolic regression methods for detecting hidden physics from sparse sensor observation

data” by H. Vaddireddy, A. Rasheed, A. E. Staples, and O. San, *Physics of Fluids*, Vol. 32 © 2020 American Institute of Physics; permission conveyed through Copyright Clearance Center, Inc.

### 5.2.3 Development of a three-dimensional computational model of the device using COMSOL Multiphysics.

As of now, we do not yet have a solid understanding of the detailed physics behind how the flow rate changes with channel design parameters as well as actuation parameters. To further understand the physics in terms of how the flow channels are differentially collapsed and re-expanded at different design and actuation parameters, there is a critical need to develop a reliable computational model. We plan to use COMSOL Multiphysics to simulate the pulse-driven flow across microfluidic channels of different design parameters. Briefly, we will first design a device geometry as shown in Figure 3.2a using COMSOL, and meshing will be used to divide the geometry into finite elements. We will separate the geometry into fluid and solid domains and apply material properties to the domains. We will generate flow by prescribing pulse parameters including actuation frequency (heart rate) and actuation pressure. Channel design parameters and pulse parameters will be varied, and responses in the flow rate will be measured.

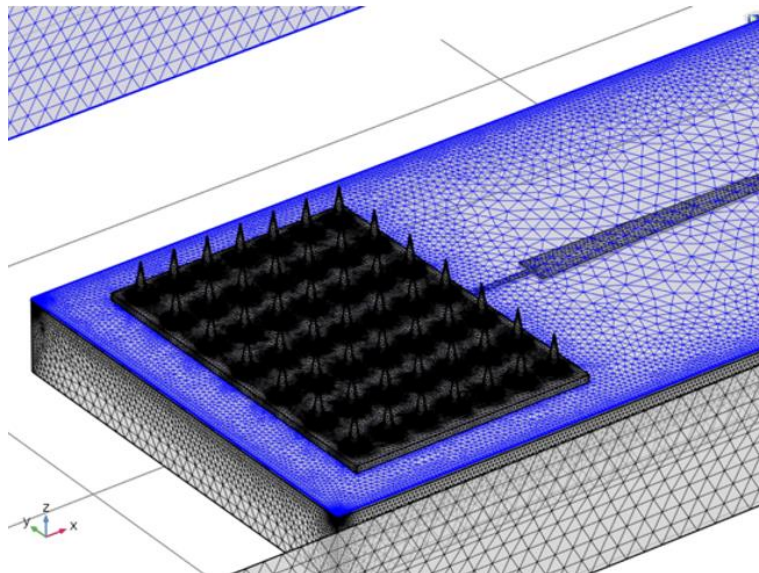


**Figure 5.3: Finite element model of microneedle array.** Finite element model by Jamie Brennan and Anne Staples.

### 5.2.4 Design and incorporation of a 3D-printed insulin reservoir.

In a practical perspective, the current components of the integrated patch-pump are still insufficient for the sustained delivery of insulin for a diabetic patient. This is because, with our

current channel design, the inside of the flow channel can only fit a few microliters of fluid, which is far from sufficient for an average diabetic patient who needs approximately 7 mg of insulin per day.<sup>101-104</sup> A slim, hollow 3D-printed insulin reservoir can be used to significantly increase the storage capacity of the system. We have designed a cubic reservoir prototype using COMSOL Multiphysics (Figure 5.4), yet the prototype is yet to be tested. The capacity of the reservoir is approximately 0.5 mL, which is more than sufficient for one day of supply for U-500 insulin.<sup>101-104</sup> As compared to regular U-100 insulin, ultraconcentrated U-500 insulin has a number of advantages. U-500 insulin has been reported to improve glycemic control of diabetic patients while increasing the adherence of patients and decreasing insulin costs due to a significant reduction in injection volume.<sup>105-107</sup> In addition, as compared to U-100 insulin, U-500 insulin results in a less sharp and more prolonged effect on blood glucose levels.<sup>108</sup> Also, the use of U-500 insulin eliminates the necessity of bulky containers due to its high insulin concentration. Considering all of these advantages, we will use U-500 insulin with a 3D-printed reservoir compatible with the microfluidic pump for efficient, continuous insulin delivery.

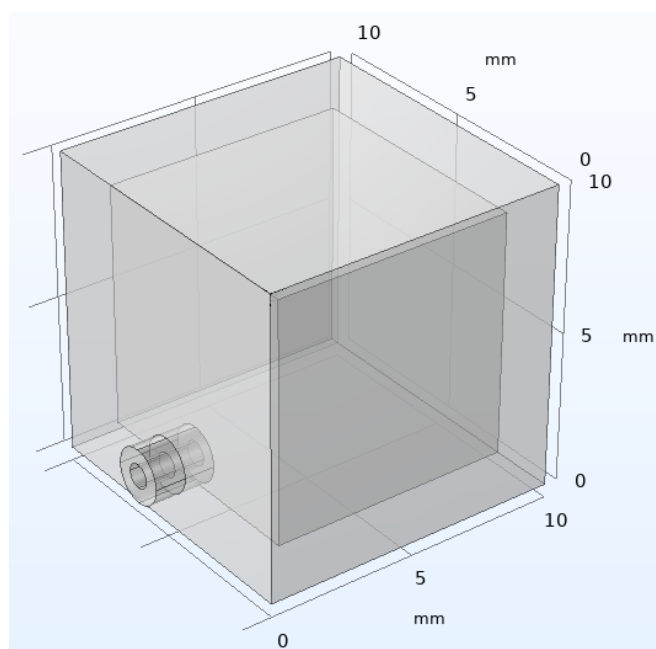


**Figure 5.4: First prototype of cubic insulin reservoir design using COMSOL Multiphysics.** This insulin reservoir has inner dimensions of  $8 \times 8 \times 8$  mm and is therefore designed to house 0.5 mL of insulin.

# Bibliography

1. Saeedi, P., Petersohn, I., Salpea, P., Malanda, B., Karuranga, S., Unwin, N., Colagiuri, S., Guariguata, L., Motala, A. A., & Ogurtsova, K. (2019). Global and regional diabetes prevalence estimates for 2019 and projections for 2030 and 2045: Results from the International Diabetes Federation Diabetes Atlas. *Diabetes research and clinical practice*, 157, 107843.
2. CDC. (2020). *National Diabetes Statistics Report: Estimates of Diabetes and Its Burden in the United States*. Retrieved April 18, 2022 from <https://www.cdc.gov/diabetes/pdfs/data/statistics/national-diabetes-statistics-report.pdf>
3. CDC. (2022). *Cost-Effectiveness of Diabetes Interventions*. Retrieved April 18, 2022 from <https://www.cdc.gov/diabetes/pdfs/data/statistics/national-diabetes-statistics-report.pdf>
4. Ozougwu, J. C., Obimba, K. C., Belonwu, C. D., & Unakalamba, C. B. (2013). The pathogenesis and pathophysiology of type 1 and type 2 diabetes mellitus. *J Physiol Pathophysiol*, 4(4), 46-57.
5. Pociot, F., & Lernmark, Å. (2016). Genetic risk factors for type 1 diabetes. *The Lancet*, 387(10035), 2331-2339.
6. Atkinson, M. A., Eisenbarth, G. S., & Michels, A. W. (2014). Type 1 diabetes. *The Lancet*, 383(9911), 69-82.
7. Akash, M. S. H., Rehman, K., & Liaqat, A. (2018). Tumor necrosis factor-alpha: role in development of insulin resistance and pathogenesis of type 2 diabetes mellitus. *Journal of cellular biochemistry*, 119(1), 105-110.
8. Bonora, E., & DeFronzo, R. (2020). *Diabetes epidemiology, genetics, pathogenesis, diagnosis, prevention, and treatment*. (A. Lenzi & E. A. Jannini, Eds.). Springer International Publishing.
9. Zheng, Y., Ley, S. H., & Hu, F. B. (2018). Global aetiology and epidemiology of type 2 diabetes mellitus and its complications. *Nature reviews endocrinology*, 14(2), 88-98.
10. Xu, G., Liu, B., Sun, Y., Du, Y., Snetselaar, L. G., Hu, F. B., & Bao, W. (2018). Prevalence of diagnosed type 1 and type 2 diabetes among US adults in 2016 and 2017: population based study. *bmj*, 362.
11. NIH National Institute of Diabetes and Digestive and Kidney Diseases. Insulin, Medicines, & Other Diabetes Treatments. Retrieved April 18, 2022 from <https://www.niddk.nih.gov/health-information/diabetes/overview/insulin-medicines-treatments>
12. Berget, C., Messer, L. H., & Forlenza, G. P. (2019). A clinical overview of insulin pump therapy for the management of diabetes: past, present, and future of intensive therapy. *Diabetes Spectrum*, 32(3), 194-204.
13. Economidou, S. N., Uddin, M. J., Marques, M. J., Douroumis, D., Sow, W. T., Li, H., ... & Podoleanu, A. (2021). A novel 3D printed hollow microneedle microelectromechanical system for controlled, personalized transdermal drug delivery. *Additive Manufacturing*, 38, 101815.

14. Bolton, C. J., Howells, O., Blayney, G. J., Eng, P. F., Birchall, J. C., Gualeni, B., ... & Guy, O. J. (2020). Hollow silicon microneedle fabrication using advanced plasma etch technologies for applications in transdermal drug delivery. *Lab on a Chip*, 20(15), 2788-2795.
15. Wang, Y., Wang, H., Zhu, X. X., Guan, Y., & Zhang, Y. (2020a). Smart microneedle patches for rapid, and painless transdermal insulin delivery. *Journal of Materials Chemistry B*, 8(40), 9335-9342.
16. Lee, B. M., Lee, C., Lahiji, S. F., Jung, U. W., Chung, G., & Jung, H. (2020). Dissolving microneedles for rapid and painless local anesthesia. *Pharmaceutics*, 12(4), 366. PMID: PMC7238259
17. Yang, J., Li, Y., Ye, R., Zheng, Y., Li, X., Chen, Y., ... & Jiang, L. (2020). Smartphone-powered iontophoresis-microneedle array patch for controlled transdermal delivery. *Microsystems & nanoengineering*, 6(1), 1-14. PMID: PMC8433361
18. Payne, F. W., Ledden, B., & Lamps, G. (2019). Capabilities of next-generation patch pump: improved precision, instant occlusion detection, and dual-hormone therapy. *Journal of Diabetes Science and Technology*, 13(1), 49-54. PMID: PMC6313296
19. Yan, B., DeLong, B., An, D., Kiourti, A., Dungan, K., Volakis, J., ... & Guo, L. (2018, March). An RF-driven lightweight implantable insulin pump. In *2018 International Applied Computational Electromagnetics Society Symposium (ACES)* (pp. 1-2). IEEE.
20. Sarbacker, G. B., & Urteaga, E. M. (2016). Adherence to insulin therapy. *Diabetes Spectrum*, 29(3), 166-170.
21. Murphy, S. L., Xu, J., & Kochanek, K. D. (2013). Deaths: final data for 2010. *National Vital Statistics Reports*, 61(4).
22. Ho, P. M., Rumsfeld, J. S., Masoudi, F. A., McClure, D. L., Plomondon, M. E., Steiner, J. F., & Magid, D. J. (2006). Effect of Medication Nonadherence on Hospitalization and Mortality Among Patients With Diabetes Mellitus. *Archives of Internal Medicine*, 166(17), 1836-1841. <https://doi.org/10.1001/archinte.166.17.1836>
23. Farsaei, S., Radfar, M., Heydari, Z., Abbasi, F., & Qorbani, M. (2014). Insulin adherence in patients with diabetes: risk factors for injection omission. *Primary care diabetes*, 8(4), 338-345.
24. Davies, M., Gagliardino, J. J., Gray, L., Khunti, K., Mohan, V., & Hughes, R. (2013). Real-world factors affecting adherence to insulin therapy in patients with Type 1 or Type 2 diabetes mellitus: a systematic review. *Diabetic Medicine*, 30(5), 512-524.
25. Kang, H., Lobo, J. M., Kim, S., & Sohn, M.-W. (2018). Cost-related medication non-adherence among US adults with diabetes. *Diabetes research and clinical practice*, 143, 24-33.
26. Arbit, E., & Kidron, M. (2017). Oral insulin delivery in a physiologic context. *Journal of diabetes science and technology*, 11(4), 825-832.
27. Gedawy, A., Martinez, J., Al-Salami, H., & Dass, C. R. (2018). Oral insulin delivery: existing barriers and current counter-strategies. *Journal of pharmacy and pharmacology*, 70(2), 197-213.
28. Mitri, J., & Pittas, A. G. (2009). Inhaled insulin—what went wrong. *Nature Clinical Practice Endocrinology & Metabolism*, 5(1), 24-25.
29. Gatto, N. M., Koralek, D. O., Bracken, M. B., Duggan, W. T., Lem, J., Klioze, S., ... & Jackson, N. C. (2019). Lung Cancer-Related Mortality With Inhaled Insulin or a

- Comparator: Follow-Up Study of patients previously enrolled in Exubera Controlled Clinical Trials (FUSE) Final Results. *Diabetes care*, 42(9), 1708-1715.
30. Oleck, J., Kassam, S., & Goldman, J. D. (2016). Commentary: why was inhaled insulin a failure in the market?. *Diabetes Spectrum*, 29(3), 180-184.
  31. Lee, H., Choi, T. K., Lee, Y. B., Cho, H. R., Ghaffari, R., Wang, L., Choi, H. J., Chung, T. D., Lu, N., & Hyeon, T. (2016). A graphene-based electrochemical device with thermoresponsive microneedles for diabetes monitoring and therapy. *Nature nanotechnology*, 11(6), 566-572.
  32. Yang, J., Chen, Z., Ye, R., Li, J., Lin, Y., Gao, J., Ren, L., Liu, B., & Jiang, L. (2018). Touch-actuated microneedle array patch for closed-loop transdermal drug delivery. *Drug delivery*, 25(1), 1728-1739. PMID: PMC6127806
  33. Chatterjee, K., Graybill, P. M., Socha, J., Davalos, R. V., & Staples, A. (2021). Frequency-specific, valveless flow control in insect-mimetic microfluidic devices. *Bioinspiration & Biomimetics*, 16(3), 036004.
  34. Aboelkassem, Y., Staples, A. E., & Socha, J. J. (2011, January). Microscale flow pumping inspired by rhythmic tracheal compressions in insects. In *Pressure Vessels and Piping Conference* (Vol. 44540, pp. 471-479).
  35. Socha, J. J., Förster, T. D., & Greenlee, K. J. (2010). Issues of convection in insect respiration: insights from synchrotron X-ray imaging and beyond. *Respiratory physiology & neurobiology*, 173, S65-S73.
  36. Yu, Y. Q., Yang, X., Wu, X. F., & Fan, Y. B. (2021). Enhancing permeation of drug molecules across the skin via delivery in nanocarriers: Novel strategies for effective transdermal applications. *Frontiers in bioengineering and biotechnology*, 9, 200.
  37. Richard, C., Cassel, S., & Blanzat, M. (2021). Vesicular systems for dermal and transdermal drug delivery. *RSC Advances*, 11(1), 442-451.
  38. Prausnitz, M. R., Mitragotri, S., & Langer, R. (2004). Current status and future potential of transdermal drug delivery. *Nature reviews Drug discovery*, 3(2), 115-124.
  39. Parhi, R., & Mandru, A. (2021). Enhancement of skin permeability with thermal ablation techniques: concept to commercial products. *Drug Delivery and Translational Research*, 11(3), 817-841.
  40. Szunerits, S., & Boukherroub, R. (2018). Heat: a highly efficient skin enhancer for transdermal drug delivery. *Frontiers in bioengineering and biotechnology*, 6, 15.
  41. Prausnitz, M. R., Bose, V. G., Langer, R., & Weaver, J. C. (1993). Electroporation of mammalian skin: a mechanism to enhance transdermal drug delivery. *Proceedings of the National Academy of Sciences*, 90(22), 10504-10508.
  42. Herndon, T. O., Gonzalez, S., Gowrishankar, T. R., Anderson, R., & Weaver, J. C. (2004). Transdermal microconduits by microscission for drug delivery and sample acquisition. *BMC medicine*, 2(1), 1-11.
  43. Li, J., Liu, B., Zhou, Y., Chen, Z., Jiang, L., Yuan, W., & Liang, L. (2017). Fabrication of a Ti porous microneedle array by metal injection molding for transdermal drug delivery. *PLoS One*, 12(2), e0172043.
  44. Luo, F. Q., Chen, G., Xu, W., Zhou, D., Li, J. X., Huang, Y. C., ... & Du, J. Z. (2021). Microneedle-array patch with pH-sensitive formulation for glucose-responsive insulin delivery. *Nano Research*, 14(8), 2689-2696.

45. Yeung, C., Chen, S., King, B., Lin, H., King, K., Akhtar, F., Diaz, G., Wang, B., Zhu, J., & Sun, W. (2019). A 3D-printed microfluidic-enabled hollow microneedle architecture for transdermal drug delivery. *Biomicrofluidics*, *13*(6), 064125. PMID: PMC6906119
46. Zhang, Y., Yu, J., Kahkoska, A. R., Wang, J., Buse, J. B., & Gu, Z. (2019). Advances in transdermal insulin delivery. *Advanced drug delivery reviews*, *139*, 51-70.
47. Ng, L. C., & Gupta, M. (2020). Transdermal drug delivery systems in diabetes management: A review. *Asian journal of pharmaceutical sciences*, *15*(1), 13-25.
48. Zhang, Y., Jiang, G., Yu, W., Liu, D., & Xu, B. (2018). Microneedles fabricated from alginate and maltose for transdermal delivery of insulin on diabetic rats. *Materials Science and Engineering: C*, *85*, 18-26.
49. Zhang, S., Poulos, D., Khoja, A., Chatterjee, K., & Staples, A. (2021). A 3D-printed microneedle array and reservoir for testing transdermal drug delivery. In *APS Division of Fluid Dynamics Meeting Abstracts* (pp. Q14-005).
50. *Permanent epoxy negative photoresist - kayaku advanced materials, inc.*. Microchem. (n.d.). Retrieved May 19, 2022, from <https://kayakuam.com/wp-content/uploads/2019/09/SU-82000DataSheet2025thru2075Ver4.pdf>
51. Chandran, K. B., Rittgers, S. E., & Yoganathan, A. P. (2012). *Biofluid mechanics : the human circulation* (2nd ed. /). CRC Press, Taylor & Francis Group. Retrieved May 8, 2022, from <https://www-taylorfrancis-com.ezproxy.lib.vt.edu/books/mono/10.1201/b11709/biofluid-mechanics>.
52. Britton, K. A., Gaziano, J. M., & Djoussé, L. (2009). Normal systolic blood pressure and risk of heart failure in US male physicians. *European journal of heart failure*, *11*(12), 1129-1134.
53. Katz, J. N., Gore, J. M., Amin, A., Anderson, F. A., Dasta, J. F., Ferguson, J. J., ... & STAT Investigators. (2009). Practice patterns, outcomes, and end-organ dysfunction for patients with acute severe hypertension: the Studying the Treatment of Acute hyperTension (STAT) registry. *American heart journal*, *158*(4), 599-606.
54. Pak, K. J., Hu, T., Fee, C., Wang, R., Smith, M., & Bazzano, L. A. (2014). Acute hypertension: a systematic review and appraisal of guidelines. *Ochsner Journal*, *14*(4), 655-663.
55. Zhang, B., Xing, C., Yu, X., Sun, B., Zhao, X., & Qian, J. (2008). Renal thrombotic microangiopathies induced by severe hypertension. *Hypertension Research*, *31*(3), 479-483.
56. White, W. B., Dey, H. M., & Schulman, P. (1989). Assessment of the daily blood pressure load as a determinant of cardiac function in patients with mild-to-moderate hypertension. *American heart journal*, *118*(4), 782-795.
57. Quer, G., Gouda, P., Galarnyk, M., Topol, E. J., & Steinhubl, S. R. (2020). Inter-and intraindividual variability in daily resting heart rate and its associations with age, sex, sleep, BMI, and time of year: Retrospective, longitudinal cohort study of 92,457 adults. *Plos one*, *15*(2), e0227709.
58. Dooley, E. E., Golaszewski, N. M., & Bartholomew, J. B. (2017). Estimating accuracy at exercise intensities: a comparative study of self-monitoring heart rate and physical activity wearable devices. *JMIR mHealth and uHealth*, *5*(3), e7043.
59. Formlabs. Elastic 50A Resin 1 L. Retrieved April 18, 2022 from [https://formlabs.com/store/materials/elastic-resin/?&utm\\_source=google&utm\\_medium=cpc&utm\\_campaign=GP\\_US-NA-Purchase-](https://formlabs.com/store/materials/elastic-resin/?&utm_source=google&utm_medium=cpc&utm_campaign=GP_US-NA-Purchase-)

- [Shopping-Store-Materials-Generic-EN-Paid-Adwords&utm\\_term=&utm\\_content=Materials&utm\\_device=c&bt=512794852549&bk=&bm=&bn=g&bg=115686595410&gclid=Cj0KCOjwmPSSBhCNARIsAH3cYgbEsvKCvruqCnSNt14QiiRGirR8i7yRPk6S8RejU6EumvfJVHR\\_VAaAo6mEALw\\_wcB](https://formlabs.com/store/flexible-80a-resin/)
60. Formlabs. Flexible 80A Resin 1 L. Retrieved April 18, 2022 from <https://formlabs.com/store/flexible-80a-resin/>
  61. Sabounchi, P., Morales, A. M., Ponce, P., Lee, L. P., Simmons, B. A., & Davalos, R. V. (2008). Sample concentration and impedance detection on a microfluidic polymer chip. *Biomedical Microdevices*, 10(5), 661-670.
  62. Graybill, P., Bollineni, R., Sheng, Z., Davalos, R., & Mirzaeifar, R. (2021). A constriction channel analysis of astrocytoma stiffness and disease progression. *Biomicrofluidics*, 15(2), 024103.
  63. Bonakdar, M., Graybill, P. M., & Davalos, R. V. (2017). A microfluidic model of the blood–brain barrier to study permeabilization by pulsed electric fields. *RSC advances*, 7(68), 42811-42818.
  64. Čemažar, J., Douglas, T. A., Schmelz, E. M., & Davalos, R. V. (2016). Enhanced contactless dielectrophoresis enrichment and isolation platform via cell-scale microstructures. *Biomicrofluidics*, 10(1), 014109. PMID: PMC4723398
  65. Shafiee, H., Caldwell, J. L., & Davalos, R. V. (2010). A microfluidic system for biological particle enrichment using contactless dielectrophoresis. *JALA: Journal of the Association for Laboratory Automation*, 15(3), 224-232.
  66. Chatterjee, K., Graybill, P., Garrett, J., Davalos, R., Socha, J., & Staples, A. (2018). Insect-inspired flow control in microfluidic networks. *Bulletin of the American Physical Society*, 63.
  67. Graybill, P. M., & Davalos, R. V. (2021, November). A Multiplexed Microfluidic Device to Measure Blood-Brain Barrier Disruption by Pulsed Electric Fields. In *2021 43rd Annual International Conference of the IEEE Engineering in Medicine & Biology Society (EMBC)* (pp. 1222-1225). IEEE.
  68. Wang, W. Y., Lin, D., Jarman, E. H., Polacheck, W. J., & Baker, B. M. (2020b). Functional angiogenesis requires microenvironmental cues balancing endothelial cell migration and proliferation. *Lab on a Chip*, 20(6), 1153-1166.
  69. Wang, W. Y., Kent III, R. N., Huang, S. A., Jarman, E. H., Shikanov, E. H., Davidson, C. D., ... & Baker, B. M. (2021a). Direct comparison of angiogenesis in natural and synthetic biomaterials reveals that matrix porosity regulates endothelial cell invasion speed and sprout diameter. *Acta Biomaterialia*, 135, 260-273.
  70. Wang, W. Y., Jarman, E. H., Lin, D., & Baker, B. M. (2021b). Dynamic Endothelial Stalk Cell–Matrix Interactions Regulate Angiogenic Sprout Diameter. *Frontiers in Bioengineering and Biotechnology*, 9, 187.
  71. Margolis, E. A., Cleveland, D. S., Kong, Y. P., Beamish, J. A., Wang, W. Y., Baker, B. M., & Putnam, A. J. (2021). Stromal cell identity modulates vascular morphogenesis in a microvasculature-on-a-chip platform. *Lab on a Chip*, 21(6), 1150-1163.
  72. Formlabs. Clear Resin 1 L. Retrieved May 18, 2022 from <https://formlabs.com/store/clear-resin/>
  73. Formlabs. Clear Resin 1 L. Retrieved May 18, 2022 from <https://formlabs.com/store/black-resin/>

74. Branski, L. K., Mittermayr, R., Herndon, D. N., Norbury, W. B., Masters, O. E., Hofmann, M., ... & Jeschke, M. G. (2008). A porcine model of full-thickness burn, excision and skin autografting. *Burns*, *34*(8), 1119-1127.
75. Formlabs | dental. Surgical Guide: A premium-quality material for printing surgical implant guides. Retrieved April 18, 2022 from <https://formlabs-media.formlabs.com/datasheets/1901234-TDS-ENUS-0.pdf>
76. Colberg, S. R., Hernandez, M. J., & Shahzad, F. (2013). Blood glucose responses to type, intensity, duration, and timing of exercise. *Diabetes care*, *36*(10), e177-e177.
77. Liu, X., Li, S., & Bao, G. (2016). Numerical simulation on the response characteristics of a pneumatic microactuator for microfluidic chips. *Journal of laboratory automation*, *21*(3), 412-422.
78. Park, J. Y., Yoo, S. J., Lee, E. J., Lee, D. H., Kim, J. Y., & Lee, S. H. (2010). Increased poly (dimethylsiloxane) stiffness improves viability and morphology of mouse fibroblast cells. *BioChip Journal*, *4*(3), 230-236.
79. Sowers, J. R. (2004). Insulin resistance and hypertension. *American Journal of Physiology-Heart and Circulatory Physiology*, *286*(5), H1597-H1602.
80. Gordon, A. M., & Mendes, W. B. (2021). A large-scale study of stress, emotions, and blood pressure in daily life using a digital platform. *Proceedings of the National Academy of Sciences*, *118*(31).
81. Munakata, M. (2018). Clinical significance of stress-related increase in blood pressure: current evidence in office and out-of-office settings. *Hypertension research*, *41*(8), 553-569.
82. Vrijkotte, T. G., Van Doornen, L. J., & De Geus, E. J. (2000). Effects of work stress on ambulatory blood pressure, heart rate, and heart rate variability. *Hypertension*, *35*(4), 880-886.
83. Hood, R. L., Kosoglu, M. A., Parker, M., & Rylander, C. G. (2011). Effects of microneedle design parameters on hydraulic resistance. *Journal of medical devices*, *5*(3).
84. Hood, R. L., Kosoglu, M. A., & Rylander, C. G. (2011, June). Hydraulic Resistance of a Novel Hollow-Core Microneedle Design. In *Summer Bioengineering Conference* (Vol. 54587, pp. 43-44). American Society of Mechanical Engineers.
85. Mata, A., Fleischman, A. J., & Roy, S. (2006). Fabrication of multi-layer SU-8 microstructures. *Journal of micromechanics and microengineering*, *16*(2), 276.
86. Rabarot, M., Bablet, J., Ruty, M., Kipp, M., Chartier, I., & Dubarry, C. (2003, January). Thick SU-8 photolithography for BioMEMS. In *Micromachining and Microfabrication Process Technology Viii* (Vol. 4979, pp. 382-393). International Society for Optics and Photonics.
87. Malekabadi, A., & Paoloni, C. (2016). UV-LIGA microfabrication process for sub-terahertz waveguides utilizing multiple layered SU-8 photoresist. *Journal of Micromechanics and Microengineering*, *26*(9), 095010.
88. Yu, J., Zhang, Y., Ye, Y., DiSanto, R., Sun, W., Ranson, D., ... & Gu, Z. (2015). Microneedle-array patches loaded with hypoxia-sensitive vesicles provide fast glucose-responsive insulin delivery. *Proceedings of the National Academy of Sciences*, *112*(27), 8260-8265.
89. Sun, X., Ji, W., Zhang, B., Ma, L., Fu, W., Qian, W., ... & Zhu, D. (2022). Theranostic microneedle array patch for integrated glycemia sensing and self-regulated release of insulin. *Biomaterials Science*, *10*, 1209-1216.

90. Ye, R., Yang, J., Li, Y., Zheng, Y., Yang, J., Li, Y., ... & Jiang, L. (2020). Fabrication of tip-hollow and tip-dissolvable microneedle arrays for transdermal drug delivery. *ACS Biomaterials Science & Engineering*, 6(4), 2487-2494.
91. Hu, X., Yu, J., Qian, C., Lu, Y., Kahkoska, A. R., Xie, Z., ... & Gu, Z. (2017). H<sub>2</sub>O<sub>2</sub>-responsive vesicles integrated with transcutaneous patches for glucose-mediated insulin delivery. *ACS nano*, 11(1), 613-620.
92. Elveflow. *Standard flow rate sensor*. Elveflow. (n.d.). Retrieved May 18, 2022, from <https://www.elveflow.com/microfluidic-products/microfluidics-flow-measurement-sensors/microfluidic-liquid-mass-flow-sensors/>
93. Kim, J., Cho, H., Han, S. I., Han, A., & Han, K. H. (2019). A disposable microfluidic flow sensor with a reusable sensing substrate. *Sensors and Actuators B: Chemical*, 288, 147-154.
94. Bombardini, T., Sicari, R., Bianchini, E., & Picano, E. (2011). Abnormal shortened diastolic time length at increasing heart rates in patients with abnormal exercise-induced increase in pulmonary artery pressure. *Cardiovascular Ultrasound*, 9(1), 1-9.
95. DeMers, D., & Wachs, D. (2020). Physiology, mean arterial pressure. In *StatPearls [Internet]*. StatPearls Publishing.
96. Razminia, M., Trivedi, A., Molnar, J., Elbזור, M., Guerrero, M., Salem, Y., ... & Lubell, D. L. (2004). Validation of a new formula for mean arterial pressure calculation: the new formula is superior to the standard formula. *Catheterization and cardiovascular interventions*, 63(4), 419-425.
97. Chemla, D., Castelain, V., Provencher, S., Humbert, M., Simonneau, G., & Hervé, P. (2009). Evaluation of various empirical formulas for estimating mean pulmonary artery pressure by using systolic pulmonary artery pressure in adults. *Chest*, 135(3), 760-768.
98. Bazan, O., & Ortiz, J. P. (2016). Duration of systole and diastole for hydrodynamic testing of prosthetic heart valves: comparison between ISO 5840 standards and in vivo studies. *Brazilian journal of cardiovascular surgery*, 31, 171-173.
99. Senger, R. S., & Nazem-Bokaei, H. (2013). Resolving cell composition through simple measurements, genome-scale modeling, and a genetic algorithm. In *Systems Metabolic Engineering* (pp. 85-101). Humana Press, Totowa, NJ.
100. Vaddireddy, H., Rasheed, A., Staples, A. E., & San, O. (2020). Feature engineering and symbolic regression methods for detecting hidden physics from sparse sensor observation data. *Physics of Fluids*, 32, 015113.
101. Reznik, Y., Cohen, O., Aronson, R., Conget, I., Runzis, S., Castaneda, J., ... & OpT2mise Study Group. (2014). Insulin pump treatment compared with multiple daily injections for treatment of type 2 diabetes (OpT2mise): a randomised open-label controlled trial. *The Lancet*, 384(9950), 1265-1272.
102. Church, T. J., & Haines, S. T. (2016). Treatment approach to patients with severe insulin resistance. *Clinical Diabetes*, 34(2), 97-104.
103. American Family Physician. (1999). Diabetes: How to Use Insulin. *American Family Physician*, 60(2), 649-651.
104. Guardian Pharmacy. (2017, April 28). *Why is insulin measured in units*. Guardian Pharmacy. Retrieved May 18, 2022, from <https://www.ptboguardian.com/single-post/2017/04/28/why-is-insulin-measured-in-units>

105. Kabul, S., Hood, R. C., Duan, R., DeLozier, A. M., & Settles, J. (2016). Patient-reported outcomes in transition from high-dose U-100 insulin to human regular U-500 insulin in severely insulin-resistant patients with type 2 diabetes: analysis of a randomized clinical trial. *Health and quality of life outcomes*, *14*(1), 1-9.
106. Eby, E. L., Wang, P., Curtis, B. H., Xie, J., Haldane, D. C., Idris, I., ... & Jackson, J. A. (2013). Cost, healthcare resource utilization, and adherence of individuals with diabetes using U-500 or U-100 insulin: a retrospective database analysis. *Journal of Medical Economics*, *16*(4), 529-538.
107. Eby, E. L., Curtis, B. H., Gelwicks, S. C., Hood, R. C., Idris, I., Peters, A. L., ... & Jackson, J. A. (2015). Initiation of human regular U-500 insulin use is associated with improved glycemic control: a real-world US cohort study. *BMJ Open Diabetes Research and Care*, *3*(1), e000074.
108. de la Peña, A., Riddle, M., Morrow, L. A., Jiang, H. H., Linnebjerg, H., Scott, A., ... & Jackson, J. A. (2011). Pharmacokinetics and pharmacodynamics of high-dose human regular U-500 insulin versus human regular U-100 insulin in healthy obese subjects. *Diabetes care*, *34*(12), 2496-2501.